A TURNING-BAND METHOD FOR THE SIMULATION OF ANISOTROPIC FRACTIONAL BROWNIAN FIELDS

HERMINE BIERMÉ [1], LIONEL MOISAN [2], AND FRÉDÉRIC RICHARD[3]

ABSTRACT. In this paper, we propose a method for simulating realizations of two-dimensional anisotropic fractional Brownian fields (AFBF) introduced by Bonami and Estrade (2003). The method is adapted from a generic simulation method called the turning-band method (TBM) due to Matheron (1973). The TBM reduces the problem of simulating a field in two dimensions by combining independent processes simulated on oriented bands. In the AFBF context, the simulation fields are constructed by discretizing an integral equation arising from the application of the TBM to non-stationary anisotropic fields. This guarantees the convergence of simulations as the step of discretization is decreased. The construction is followed by a theoretical study of the convergence rate (the detailed proofs are available in the online Supplementary Materials). Another key feature of this work is the simulation of band processes. Using self-similarity properties, processes are simulated exactly on bands with a circulant embedding method, so that simulation errors are exclusively due to the field approximation. Moreover, we design a Dynamic Programming algorithm that selects band orientations achieving the optimal trade-off between computational cost and precision. Finally, we conduct a numerical study showing that the approximation error does not significantly depend on the regularity of the fields to be simulated, nor on their degree of anisotropy. Experiments also suggest that simulations preserve the statistical properties of the original field.

1. INTRODUCTION

The famous fractional Brownian motion (FBM) was introduced by Kolmogorov (1940) and Mandelbrot and Van Ness (1968) for the modeling of irregular one-dimensional data

2010 *Mathematics Subject Classification.* 60G60; 60G22; 60-04.

Key words and phrases. Turning bands; simulation; fractional Brownian field; Gaussian field; anisotropy; non-stationarity; stationary increments.

exhibiting scale invariance and characterized by a single parameter $H \in (0,1)$, called Hurst parameter. Several extensions have been proposed for 2-dimensional data accounting for spatial correlations. Among them, fractional Brownian fields (FBF) are natural extensions that preserve the two main properties of FBM, namely stationary increments and self-similarity. However, such fields are isotropic in the sense that their law is invariant under rotation, which is a serious drawback for many applications. For the modeling and analysis of the anisotropy of image textures, Anisotropic Fractional Brownian Fields (AFBF) were introduced by Bonami and Estrade (2003) (see the definition in Section 2.1) and were applied in medical imaging for the analysis of mammogram and bone radiograph textures (Biermé and Richard, 2009). The main features of the AFBF model are stationary increments and two orientation-dependent functional parameters c and h, called respectively the topothesy (Davies and Hall, 1999) and Hurst functions. Due to these parameters, the AFBF model covers a wide range of textures having different types of anisotropies. When the Hurst function is constant, the model describes a large class of self-similar random fields whose anisotropy is characterized by the topothesy function. When the Hurst function also varies, the field may no longer be strictly self-similar, but only asymptotically self-similar. This allows one to fit realistic textures having different properties at small and large scales, *e.g.* showing irregular patterns on a smooth heterogeneous background.

The simulation of AFBF is an open issue whose complexity is mainly due to both the non-stationarity and the anisotropy of the fields. Stein (2002) described a specific method for the simulation of (isotropic) FBF. This method is based on a representation of the FBF by a locally stationary isotropic Gaussian field, which is simulated using circulant embedding matrix techniques developed by Dietrich (1995) and Wood and Chan (1994). This simulation is exact and efficient on a regular grid. However, since there is not any locally stationary representation for general anisotropic fields, Stein's method cannot be extended to the simulation of these fields.

More generic methods based on covariance matrix factorizations (Brouste *et al.*, 2007; Chan, 1999) cannot be applied to AFBF. In theory, they require covariance functions to be explicitly known (which is not the case for the AFBF) and in practice, their computational cost is prohibitive. Other methods based on the discretization of a continuous spectral representation of the field were used for the simulation of FBF by Saupe (1988) and AFBF by Ayache *et al.* (2005) and Biermé and Richard (2008). However, due to the truncation and periodization of the spectral representation, the statistical properties of the simulated field do not exactly match those of the theoretical field.

In this paper, we focus on another generic simulation method, called the turning-band method (TBM) (Matheron, 1973; Journel, 1974), which is more adapted to AFBF simulations. The TBM essentially reduces the problem of simulating a field in several dimensions to the problem of simulating several processes in one dimension. Indeed, consider the problem of generating a realization of a target field X on a discrete set G of points of $\mathbb{R}^2$. Choose n lines (called turning bands) passing through a given origin and denote by θ_i the angle indicating the direction of the ith band. The TBM is based on n appropriate processes $(Y_i)_{1\leq i\leq n}$ independently simulated on each predefined band, that are linearly combined to build the field

$$X_n(x) = \sum_{i=1}^{n} \sqrt{\lambda_i}\, Y_i(x \cdot u(\theta_i)), \quad x \in G \tag{1}$$

where the λ_i's are positive weights, $u(\theta) = (\cos(\theta), \sin(\theta))$ is a unit vector with direction θ, and $u \cdot v$ denotes the usual inner product in $\mathbb{R}^2$.

There are two major issues raised by the application of the TBM. The first one consists of determining appropriate weights λ_i and band processes Y_i which ensure the convergence of the turning-band field X_n to the target field X as n tends to infinity. The second one concerns the simulation of the processes Y_i on the non-equispaced points $\{x \cdot u(\theta_i), x \in G\}$.

The convergence issue has been extensively studied in the case when the target field is stationary (Brooker, 1985; Christakos, 1987; Dietrich, 1995; Gneiting, 1996, 1998; Mantoglou, 1987; Matheron, 1973). In this case, the convergence can be obtained using

stationary band processes. The TBM has also been adapted to the simulation of non-stationary fields with stationary increments (Dimitrakopoulos, 1990; Chilès and Delfiner, 2012; Emery, 2008; Mantoglou and Wilson, 1982; Matheron, 1973; Pardo-Igúzquiza and Dowd, 2003). In such a situation, the convergence of the turning-band field to the target one is expressed in terms of semi-variograms instead of covariances. It is obtained by taking band processes with stationary increments and semi-variograms $\tilde{v}_\theta$ (in the direction θ) which satisfy the condition

$$v_X(y) = \int_{-\frac{\pi}{2}}^{\frac{\pi}{2}} \tilde{v}_\theta(y \cdot u(\theta))\, d\theta, \tag{2}$$

where v_X is the semi-variogram of the target field X (see Equation (3) below). In this paper, we show that AFBF satisfy this equation for the semi-variograms $\tilde{v}_\theta$ of non-standard FBMs, whose Hurst exponent and topothesy parameter depend on the direction θ.

Consequently, the TBM algorithm for AFBF requires the simulation of one-dimensional FBM. In the isotropic case of FBF, TBM algorithms have already been developed. Yin (1996) proposes to simulate the FBM band processes using the spectral method (Mantoglou and Wilson, 1982; Pardo-Igúzquiza and Chica-Olmo, 1993; Shinozuka and Jan, 1972), while Emery (2008) synthetizes them using random cosine functions. In both cases, the band processes are non-Gaussian, and not self-similar processes. Simulations are only asymptotically Gaussian due to a Central Limit Theorem.

One of the main originalities of the present paper is the construction of an appropriate turning-band field that simulates the AFBF while keeping its main statistical properties: Gaussianity, stationary increments, and (asymptotical) self-similarity. This construction relies upon a technique we develop for the exact simulation of the FBM on non-uniformly spaced points. This technique is an extension of the circulant embedding method introduced in (Dietrich and Newsam, 1997; Wood and Chan, 1994) and already used in (Perrin *et al.*, 2002) for the simulation of FBM on equispaced points.

The application of this extended technique in the AFBF simulation context has a computational cost which mainly depends on band orientations and is higher than the

one of the continuous spectral method in Emery (2008) and Emery and Lantuéjoul (2006). To reduce this cost, we thus propose a Dynamic Programming algorithm (Bellman, 1954) that selects band orientations in an optimal way.

Furthermore, the construction of the AFBF simulation method is completed by theoretical and numerical analyses of the simulation error. These analyses bring new insights into the TBM simulation error, which has been mainly investigated in the stationary isotropic case (Chilès, 1977; Gneiting, 1998; Mantoglou and Wilson, 1982).

2. The turning-band method

2.1. **Anisotropic fractional Brownian fields.** Let $(\Omega, \mathcal{A}, \mathbb{P})$ be a probability space. A 2-dimensional random field X is a map from $\Omega \times \mathbb{R}^2$ into $\mathbb{R}$ such that $X(\cdot, y)$ (shortly written $X(y)$) is a real random variable on Ω for all $y \in \mathbb{R}^2$. A random field is Gaussian if any finite linear combination of its associated random variables is a Gaussian variable. A centered Gaussian field X is characterized by its covariance function: $(y, z) \mapsto \mathrm{Cov}(X(y), X(z))$. A field X has stationary increments if the law governing the field $X(\cdot + z) - X(z)$ is the same as $X(\cdot) - X(0)$ for all $z \in \mathbb{R}^2$. When the field X is centered and has stationary increments, one has $\forall y, z \in \mathbb{R}^2$, $\mathrm{Cov}(X(y) - X(0), X(z) - X(0)) = v_X(y) + v_X(z) - v_X(y - z)$, where v_X is the so-called semi-variogram of X defined as

$$\forall y \in \mathbb{R}^2, \quad v_X(y) = \frac{1}{2}\mathbb{E}((X(y) - X(0))^2). \tag{3}$$

Hence, if the field X is also Gaussian with $X(0) = 0$ a.s., its law is characterized by its semi-variogram (3). From a generalization of Bochner Theorem, a function v is the semivariogram of a 2-dimensional Gaussian random field if and only if there exists a Lévy measure μ, i.e. a positive Borel measure satisfying $\int_{\mathbb{R}^2} \min(1, |\zeta|^2)\mu(d\zeta) < +\infty$, such that

$$\forall\, x \in \mathbb{R}^2, \quad v(x) = \frac{1}{2}\int_{\mathbb{R}^2} \left|e^{ix\cdot\zeta} - 1\right|^2 \mu(d\zeta). \tag{4}$$

When $\mu(d\zeta) = f(\zeta)d\zeta$, the positive function f is called a spectral density. In this work, we deal with anisotropic fractional Brownian fields, which are centered Gaussian fields

with stationary increments, characterized by a a spectral density of the form

$$\forall\, \zeta \in \mathbb{R}^2, \quad f(\zeta) = c(\arg(\zeta))\, |\zeta|^{-2h(\arg(\zeta))-2}, \tag{5}$$

where $|\zeta|$ is the Euclidean norm of ζ, $\arg(\zeta)$ is the direction of ζ, and a semi-variogram of the form (4) with $\mu(d\zeta) = f(\zeta)d\zeta$. Functions c and h, called topothesy and Hurst functions, are two π-periodic measurable functions, defined on $(-\pi/2, \pi/2]$, with ranges satisfying $c((-\pi/2, \pi/2]) \subset \mathbb{R}^+$ and $h((-\pi/2, \pi/2]) \subset (0, 1)$ to ensure that μ is a Lévy measure. When $c \equiv C > 0$ and $h \equiv H \in (0, 1)$ are both constant, the semi-variogram satisfies (see Lacaux (2004, Remark 1.1.13) for instance)

$$v(x) = \frac{1}{2} \int_{\mathbb{R}^2} \left|e^{ix\cdot\zeta} - 1\right|^2 C|\zeta|^{-2H-2} d\xi = C \frac{\pi^{\frac{1}{2}}\Gamma(H + 1/2)\gamma(H)}{2\Gamma(H + 1)} |x|^{2H}, \tag{6}$$

$$\text{where} \qquad \forall H \in (0, 1), \quad \gamma(H) = \frac{\pi}{H\Gamma(2H)\sin(H\pi)}. \tag{7}$$

It follows that such fields are isotropic, which means that their law is invariant under rotation. They are also H-self-similar meaning that the law governing the field $X(\lambda\,\cdot)$ is the same as $\lambda^H X(\cdot)$ for all $\lambda \in \mathbb{R}$. When the function c is not constant but h remains constant ($h \equiv H$), the field remains self-similar of order H but becomes anisotropic. When h is also allowed to vary, the field is not self-similar anymore but asymptotically of order $H = \operatorname*{ess\,inf}_{\theta \in S^{d-1};\, c(\theta)>0} h(\theta)$, as shown by Bonami and Estrade (2003, Proposition 2).

In general, it is difficult to get an explicit form of the AFBF semi-variogram similar to the one expressed in (6) for the FBF. However, we have computed explicitly the semi-variogram of a particular class of AFBF which is slightly more general than the FBF (see online Supplementary Materials, Appendix A, Proposition 1). This field, which we call an elementary field, is defined by a spectral density of the form (5) with $c = \mathbf{1}_{[\alpha_1,\alpha_2]}$ for $-\pi/2 \leq \alpha_1 < \alpha_2 \leq \pi/2$ and $h \equiv H$ for $H \in (0, 1)$. It is therefore H-self-similar. Moreover, when $\alpha_2 = -\alpha_1 = \pi/2$, an elementary field corresponds to an isotropic FBF of order H. However, in the general case when $\alpha_2 - \alpha_1 < \pi$, the corresponding elementary field is anisotropic. As explained in Section 4, elementary fields will be of particular

interest for the numerical evaluation of simulations. Now, let us consider the general case from which the TBM will follow.

2.2. **Turning-band fields for AFBF.** By a change of variables in polar coordinates, we derive an integral expression for the semi-variogram of an AFBF.

Proposition 2.1. *Let X be a centered Gaussian field with stationary increments with $X(0) = 0$ a.s. Let us assume that its semi-variogram v_X is of the form (4) with a spectral density defined by (5) with c and h two π-periodic measurable functions with ranges satisfying $c((-\pi/2, \pi/2]) \subset \mathbb{R}^+$ and $h((-\pi/2, \pi/2]) \subset (0, 1)$. Then, for all $x \in \mathbb{R}^2$,*

$$v_X(x) = \frac{1}{2} \int_{-\pi/2}^{\pi/2} \gamma(h(\theta)) c(\theta) |x \cdot u(\theta)|^{2h(\theta)} d\theta, \tag{8}$$

where $u(\theta) = (\cos(\theta), \sin(\theta))$ and $\gamma(\cdot)$ is defined in Equation (7).

Proof. Let $x \in \mathbb{R}^2$. Then according to (4) and (5),

$$\begin{aligned} 2v_X(x) &= \int_{\mathbb{R}^2} \left| e^{ix\cdot\zeta} - 1 \right|^2 c(\arg(\zeta)) |\zeta|^{-2h(\arg(\zeta))-2} d\zeta \\ &= \int_0^{2\pi} \int_0^{+\infty} \left| e^{ir(x\cdot u(\theta))} - 1 \right|^2 c(\theta) r^{-2h(\theta)-1} dr d\theta, \end{aligned}$$

by a change of variables in polar coordinates. But, for $H \in (0, 1)$ and $t \in \mathbb{R}$,

$$\int_0^{+\infty} \left| e^{irt} - 1 \right|^2 r^{-2H-1} dr = \frac{1}{2} \int_{\mathbb{R}} \left| e^{ist} - 1 \right|^2 |s|^{-2H-1} ds = \frac{1}{2} \gamma(H) |t|^{2H},$$

according to (7.2.13) of Samorodnitsky and Taqqu (1994). Then the result follows by π-periodicity of h and c. □

The integral equation (8) above is of the form (2) with $\tilde{v}_\theta(\cdot) = \gamma(h(\theta)) c(\theta) \frac{1}{2} |\cdot|^{2h(\theta)}$. This means that $\tilde{v}_\theta$ is a solution of the integral equation (2) when v_X is the semi-variogram of an AFBF. Now recall that a standard FBM of order H is a centered Gaussian process with stationary increments and semi-variogram $w_H(t) = \frac{1}{2}|t|^{2H}$ for all $t \in \mathbb{R}$. Hence, up to the factor $\gamma(h(\theta))c(\theta)$ depending only on the orientation θ, the semi-variogram $\tilde{v}_\theta$ is equal to the one of a FBM of order $h(\theta)$, also varying with θ.

According to previous remarks, we now specify turning-band fields for AFBF simulations. Given an ordered set $\Theta = (\theta_i)_{1\leq i\leq n}$ of band orientations $-\pi/2 \leq \theta_1 < \ldots < \theta_n \leq \pi/2$, and a set $\Lambda = (\lambda_i)_{1\leq i\leq n} \in [0,+\infty)^n$ of appropriate band weights, a turning-band field has the form

$$X_{\Theta,\Lambda}(x) = \sum_{i=1}^{n} \sqrt{\lambda_i \gamma(h(\theta_i)) c(\theta_i)}\, Y_i(x \cdot u(\theta_i)),\ \forall x \in \mathbb{R}^2, \tag{9}$$

where the Y_i's are n independent FBM of order $h(\theta_i)$. Its semi-variogram has the form

$$v_{\Theta,\Lambda}(x) := \sum_{i=1}^{n} \lambda_i \gamma(h(\theta_i))\, c(\theta_i)\, w_{h(\theta_i)}(x \cdot u(\theta_i)). \tag{10}$$

Let us emphasize that the turning-band field $X_{\Theta,\Lambda}$ is a centered Gaussian random field with stationary increments with $X_{\Theta,\Lambda}(0) = 0$ a.s. Moreover, when $h \equiv H$, it is also self-similar of order H. Therefore $X_{\Theta,\Lambda}$ shares the same law properties as X.

In the remaining text, a turning-band field $X_{\Theta,\Lambda}$ will be called the simulation field, and the process Y_i will always be a FBM of order $h(\theta_i)$. We will also describe the precision of a simulation field $X_{\Theta,\Lambda}$ using the quantity

$$\varepsilon_\Theta = \max_{i=1,\cdots,n+1} (\theta_i - \theta_{i-1}), \tag{11}$$

where $\theta_0 \in [-\pi/2, \theta_1]$ and $\theta_{n+1} \in [\theta_n, \pi/2]$ are fixed directions chosen according to the AFBF function c. When orientations are selected uniformly in $(-\pi/2, \pi/2)$, $\varepsilon_\Theta = \pi/n$. In general, $\varepsilon_\Theta \geq \frac{\theta_n - \theta_0}{n} \geq \frac{\theta_n - \theta_1}{n}$, which links the precision ε_Θ to the number of lines.

The error of simulating X by $X_{\Theta,\Lambda}$ may be expressed, at point $x \in \mathbb{R}^2$, as the Kolmogorov distance between the random variables $X_{\Theta,\Lambda}(x)$ and $X(x)$, that is,

$$d_{Kol}(X_{\Theta,\Lambda}(x), X(x)) = \sup_{t\in\mathbb{R}} \left|\mathbb{P}(X_{\Theta,\Lambda}(x) \leq t) - \mathbb{P}(X(x) \leq t)\right|. \tag{12}$$

When this distance tends to 0, it implies that the random variable $X_{\Theta,\Lambda}(x)$ tends to $X(x)$ in distribution. As stated next, due to our Gaussian framework, this distance can be further bounded by a distance between semi-variograms of simulation and target fields.

Theorem 2.2. *Let $X_{\Theta,\Lambda}$ be a simulation field defined as in Equation (9). Then, $X_{\Theta,\Lambda}$ is a centered Gaussian random field on $\mathbb{R}^2$ with stationary increments and semi-variogram given by Equation (10). Moreover, $X_{\Theta,\Lambda}(0) = X(0) = 0$ a.s. and, for all $x \neq 0$,*

$$d_{Kol}(X_{\Theta,\Lambda}(x), X(x)) \leq 2\frac{|v_X(x) - v_{\Theta,\Lambda}(x)|}{v_X(x)}. \tag{13}$$

If $(\Theta_n, \Lambda_n)_n$ is chosen in such a way that $v_{\Theta_n,\Lambda_n}(x) \underset{n\to+\infty}{\longrightarrow} v_X(x)$ for all $x \in \mathbb{R}^2$, then $(X_{\Theta_n,\Lambda_n}(x))_{x\in\mathbb{R}^2}$ converges to $(X(x))_{x\in\mathbb{R}^2}$, in the sense of finite dimensional distributions.

The proof is given in the online Supplementary Materials (Appendix A, Section 2). Let us note that, since $v_{\Theta,\Lambda}$ appears as a numerical approximation of the integral giving v_X, one can choose $(\Theta_n, \Lambda_n)_n$ in such a way that $v_{\Theta_n,\Lambda_n}(x)$ tends to $v(x)$ for $x \in \mathbb{R}^2$. This implies that $d_{Kol}(X_{\Theta_n,\Lambda_n}(x), X(x)) \to 0$ so that $X_{\Theta_n,\Lambda_n}(x)$ tends to $X(x)$ in distribution. Note that conversely, since $X_{\Theta_n,\Lambda_n}(x)$ and $X(x)$ are centered Gaussian variables, $v_{\Theta_n,\Lambda_n}(x)$ tends to $v(x)$ as soon as $X_{\Theta_n,\Lambda_n}(x)$ tends to $X(x)$ in distribution. The next section is devoted to the analysis of the convergence rate.

2.3. **Approximation error.** Under appropriate regularity assumptions on c and h, we can choose Θ and Λ so that the bound in the right-hand term of (13) holds uniformly on a compact set. A first result can be established for elementary fields (see online Supplementary Materials, Appendix A, Section 3), then generalized to piecewise $\mathcal{C}^1$ Hurst and topothesy functions.

Proposition 2.3. *Assume that h and c are piecewise $\mathcal{C}^1$ on $(-\pi/2, \pi/2]$ and write*

$$H = \min_{\theta\in[-\pi/2,\pi/2]} h(\theta) \in (0, 1). \tag{14}$$

Let $\Theta = (\theta_i)_{1\leq i\leq n}$ with $-\pi/2 \leq \theta_1 < \ldots < \theta_n \leq \pi/2$ containing the singular points of h and c and ε_Θ given by (11) with $\theta_0 \in [-\pi/2, \theta_1]$, $\theta_{n+1} \in [\theta_n, \pi/2]$. Let T be a compact set of $\mathbb{R}^2$. Then, one can find $\Lambda = (\lambda_i)_{1\leq i\leq n} \in [0, +\infty)^n$ and a positive constant $C_T > 0$, independent of Θ, Λ, such that for all $x \in T$,

$$|v_X(x) - v_{\Theta,\Lambda}(x)| \leq C_T \varepsilon_\Theta^{\min(2H,1)}. \tag{15}$$

If moreover, h and c are piecewise $\mathcal{C}^2$ on $(-\pi/2, \pi/2]$, one can find $\Lambda = (\lambda_i)_{1\leq i\leq n} \in [0,+\infty)^n$ and a positive constant $C_T > 0$, independent of Θ, Λ, such that for all $x \in T$,

$$|v_X(x) - v_{\Theta,\Lambda}(x)| \leq C_T \begin{cases} \left(\varepsilon_\Theta^3 \delta_\Theta^{-2+\min(2H,1)} + \varepsilon_\Theta^{1+\min(2H,1)}\right) & \text{if } H \neq 1/2, \\ \left(\varepsilon_\Theta^3 \delta_\Theta^{-1} |\log(\delta_\Theta)| + \varepsilon_\Theta^2\right) & \text{if } H = 1/2 \end{cases} \tag{16}$$

with $\delta_\Theta = \min_{1\leq i\leq n-1} (\theta_{i+1} - \theta_i)$.

The proof of Proposition 2.3 is given in the online Supplementary Materials (Appendix A, Section 4). In conjunction with Theorem 2.2, it gives a practical way to control the approximation error associated with a given choice of Θ, since the Kolmogorov distance between the theoretical field X and the simulated field $X_{\Theta,\Lambda}$ can be bounded from above thanks to (13) and (16). In practice, the values Θ are approximately equispaced (see Section 3.2 for a discussion on the choice of Θ), so that the values of ε_Θ and δ_Θ are close and inversely proportional to the number of bands n, and the bound in (16) behaves like $1/n^2$ if $H < 1/2$, like $\log(n)/n^2$ if $H = 1/2$, and like $1/n^{1+2H}$ if $H > 1/2$.

For the particular case of elementary fields, explicit examples of weights (based on rectangular or trapezoidal integral approximation) are given in Appendix A. Moreover, due to self-similarity, the previous proposition is strongly improved since the uniform bound actually holds for the Kolmogorov distance itself (see Proposition 4 in Appendix A). Note also that, due to discretization, $X_{\Theta,\Lambda}$ may be considered as a linear combination of independent approximations of elementary fields.

As a comparison, Emery and Lantuéjoul (2008) also propose a TBM to synthesize an isotropic FBF (say X), which actually corresponds to an elementary field with $\alpha_1 = -\pi/2$ and $\alpha_2 = \pi/2$. However, the processes simulated on the bands are not Gaussian so that the Kolmogorov distance between the simulated random variable and the (elementary) field X is bounded by the Berry Esseen bound given by $n^{-1/2}$, with n the number of bands (see Equation (27) in Emery and Lantuéjoul (2008)). This bound is to be compared with the $1/n^2$, $\log(n)/n^2$ and $1/n^{1+2H}$ bounds (according to the value of H) mentioned after

Proposition 2.3. Moreover, in their approach the distance also depends on the point $x \in \mathbb{R}^2$, which is not the case in the present work (see Appendix A, Proposition 4).

The next section is devoted to the exact simulation of $X_{\Theta,\Lambda}$ on the discrete grid $r^{-1}\mathbb{Z}^2 \cap [0,1]^2$ for some $r \geq 1$, for conveniently chosen Θ. This relies on fast and exact synthesis of band processes on the corresponding involved points.

3. Fast and exact simulation on bands

3.1. **Choice of bands.** We consider the exact simulation of $X_{\Theta,\Lambda}$ on the discrete grid $r^{-1}\mathbb{Z}^2 \cap [0,1]^2$ for some $r \geq 1$. Then for any i with $1 \leq i \leq n$ we have to simulate on each band of direction $u(\theta_i)$

$$\left\{Y_i(x \cdot u(\theta_i)); x \in r^{-1}\mathbb{Z}^2 \cap [0,1]^2\right\} = \left\{Y_i\left(\frac{k_1}{r}\cos(\theta_i) + \frac{k_2}{r}\sin(\theta_i)\right); 0 \leq k_1, k_2 \leq r\right\}.$$

Note that when $\theta_i = \pi/2$ we can simply use the fact that $\left\{Y_i\left(\frac{k_2}{r}\right); 0 \leq k_2 \leq r\right\} \stackrel{d}{=} r^{-h(\theta_i)}\left\{Y_i\left(k_2\right); 0 \leq k_2 \leq r\right\}$, by self-similarity. When $\cos(\theta_i) \neq 0$ we may choose θ_i such that $\tan\theta_i = \frac{p_i}{q_i}$, with $p_i \in \mathbb{Z}$ and $q_i \in \mathbb{N}\setminus\{0\}$. But, $\left\{Y_i\left(\frac{k_1}{r}\cos(\theta_i) + \frac{k_2}{r}\sin(\theta_i)\right); 0 \leq k_1, k_2 \leq r\right\}$ has the same law as $\left(\frac{\cos(\theta_i)}{rq_i}\right)^{h(\theta_i)}\left\{Y_i\left(k_1 q_i + k_2 p_i\right); 0 \leq k_1, k_2 \leq r\right\}$. Thus, the band with direction $u(\theta_i)$ involves the simulation of a 1D FBM on a discrete interval of length $r(|p_i| + q_i)$. According to Perrin *et al.* (2002), one can get a fast and exact synthesis using the circulant embedding method. The computational cost of this simulation is $C(r(|p_i| + q_i))$, where $C(rl)$ is the computational cost of the method described in the online Supplementary Materials (Appendix A, Section 5) to simulate a 1D FBM on the discrete interval $\{0, \ldots, rl\}$. If the Fast Fourier Transform with powers of two is used, then $C(rl) = O(2^{\lceil \log_2(rl)\rceil}\lceil \log_2(rl)\rceil)$, where $\lceil x\rceil$ denotes the upper integer part of x. Finally, the overall simulation process has to find a trade-off between the computational cost

$$\mathcal{C}(\Theta) = \sum_i C(r(|p_i| + q_i)) \tag{17}$$

and the precision of the simulation, which is controlled by $\mathcal{E}(\Theta) = \varepsilon_\Theta^{\min(2H,1)}$, with H given by (14). The optimal choice of Θ is discussed in the following section.

3.2. **Band selection by Dynamic Programming.** We would like to minimize the computational cost $\mathcal{C}(\Theta)$ over all angle sets Θ such that $\varepsilon_\Theta \leq \varepsilon$ (ε being a given precision parameter). As we saw above, the angles $\theta \in \Theta$ must have a rational tangent, so that one can find an integer N (large enough) such that each angle θ of an optimal solution Θ can be written under the form $\theta = \arctan \frac{p}{q} \in [-\frac{\pi}{2}, \frac{\pi}{2}]$, where (p, q) belongs to

$$\mathcal{V}_N = \left\{ (p,q);\ -N \leq p \leq N, 1 \leq q \leq N, \gcd(p,q) = 1, \alpha_1 < \arctan \frac{p}{q} < \alpha_2 \right\}. \tag{18}$$

Of course, exploring all subsets of $\mathcal{V}_N$ is not possible in a reasonable time, but it turns out that the combinatorial minimization problem we are considering,

$$\min \mathcal{C}(\Theta) \text{ under the constraints } \Theta \in \mathcal{P}\left(\left\{ \arctan \frac{p}{q}; (p,q) \in \mathcal{V}_N \right\} \right),\ \varepsilon_\Theta \leq \varepsilon \tag{19}$$

has a recursive structure that can be exploited to design an efficient *exact* algorithm with polynomial complexity. This class of algorithms is referred to as Dynamic Programming (Bellman, 1954) and is commonly used for graph optimization problems.

We now describe the Dynamic Programming algorithm that can be used to solve (19). Assume that the set $\mathcal{V}_N$ has been sorted into a sequence $(p_k, q_k)_{1 \leq k \leq n}$ such that the associated angular sequence $\theta_k = \arctan \frac{p_k}{q_k}$ is increasing. Writing $e_k = C(r(|p_k| + q_k))$ for the elementary cost associated with a band of orientation θ_k, we can rewrite the total computational cost of a set of angles $\Theta = (\theta_{i_k})_{1 \leq k \leq s}$ as $C(\Theta) = \sum_{k=1}^{s} e_{i_k}$. We add the convention that $\theta_{n+1} = \alpha_2$ and $\theta_0 = \alpha_1$ (with the associated elementary cost $e_0 = 0$). Now, for $0 \leq i \leq n+1$, let us call c_i the minimal cost that can be realized with a sequence $i_1 = i, i_2, \ldots i_s = n+1$ for some integer s. Then, c_0 is the optimal cost we look for, and for all $0 \leq i \leq n$ we have $c_i = e_i + \min_{j;\, j>i,\, \theta_j \leq \theta_i + \varepsilon} c_j$. This induction formula (called the Bellman Equation in the framework of Dynamic Programming) permits us to compute the optimal costs $c_n, c_{n-1}, \ldots c_0$ recursively (the initialization being made with $c_{n+1} = 0$). Moreover, each time the minimum in Bellman Equation is computed, we consider one optimal index $k_i \in \arg\min_{j;\, j>i,\, \theta_j \leq \theta_i + \varepsilon} c_j$, so that an optimal sequence $i_1, i_2, \ldots i_s$ can be computed by tracking back indexes that achieve the optimal cost c_0. This sequence

is given by $i_1 = k_0, i_2 = k_{i_1}, \dots i_s = k_{i_{s-1}}$, where the value of s is obtained using the fact that $i_{s+1} = n + 1$. In the end, the desired sequence of integer vectors is simply $(\bar{p}_k, \bar{q}_k)_{1 \leq k \leq s}$, where $(\bar{p}_k, \bar{q}_k) = (p_{i_k}, q_{i_k})$ for all $1 \leq k \leq s$. The whole procedure we just described is given in pseudo-code in the online Supplementary Materials, Appendix B. In practice, it seems that choosing $N = 1 + \left\lceil \frac{1}{\tan \varepsilon} \right\rceil$ (which ensures that the constraint $\varepsilon_\Theta \leq \varepsilon$ is feasible) is sufficient to achieve the optimal solution, though we do not have a proof of this (even if this were not true, the algorithm we present here would yield slightly sub-optimal sets of bands, with little practical consequences). In Figure 1, the Dynamic

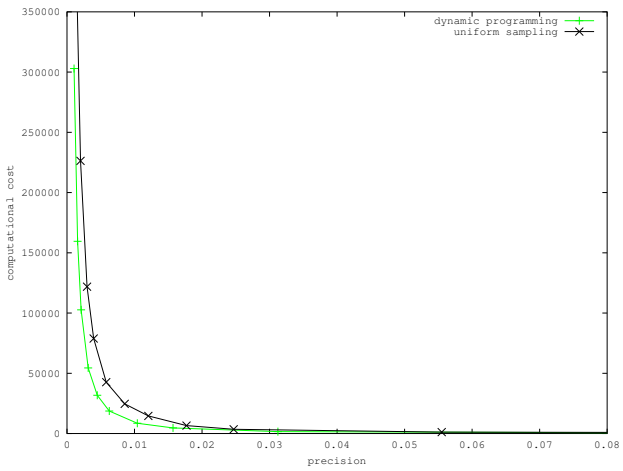

FIGURE 1. Computational cost achieved with a pseudo-uniform sampling of the turning bands versus their selection by Dynamic Programming.

Programming algorithm we described is compared to a pseudo-uniform sampling of Θ, where each $\theta_i = \arctan \frac{p_i}{q_i}$ is computed by choosing for each i an appropriate convergent p_i/q_i of the continued fraction associated with $\tan\left(\alpha_1 + \frac{i}{n}(\alpha_2 - \alpha_1)\right)$. It appears that the proposed Dynamic Programming algorithm achieves a significantly lower computational cost. Note that choosing the number n of bands as $1/\varepsilon$ with ε the precision parameter, the TBM involves the computation of n 1D FFTs of vectors whose size is of the order $n \times r$, where r is the step of the discrete grid.

4. Numerical Study

This section is devoted to the numerical evaluation of anisotropic fractional Brownian field (AFBF) simulations obtained by turning bands.

Let us recall some notations. The field X is the theoretical field to be simulated (AFBF). Its semi-variogram v_X is of the form (4) with a spectral density defined by (5). The field $X_{\Theta,\Lambda}$ is the turning-band simulation field defined by Equation (9) for some sets Θ and Λ giving band orientations and weights, respectively. The semi-variogram $v_{\Theta,\Lambda}$ of $X_{\Theta,\Lambda}$ is defined by Equation (10).

In all experiments, the set Θ of band orientations was computed automatically using the Dynamic Programming algorithm described in Section 3.2 with a constraint on field precision. The precision parameter ε_Θ associated with the set Θ is defined as in Equation (11). Weights λ_i of Λ are defined to fulfill the condition of Proposition 4 (see online Supplementary Materials, Appendix A, Section 3).

4.1. **The use of elementary fields.**

Our evaluation is based on elementary fields whose spectral density is given by Equation (5) taking $h \equiv H$ for some $H \in (0,1)$ and $c = \mathbf{1}_{[-\alpha,\alpha]}$ for some $0 < \alpha \leq \pi/2$.

Elementary fields are specified by only two parameters, H and α, which can be interpreted as regularity and anisotropy parameters, respectively. The Hölder regularity of these fields being equal to H (see Bonami and Estrade (2003) for instance), it increases as H tends to 1. When $\alpha = \pi/2$, the elementary field corresponds to the usual isotropic fractional Brownian field with Hurst index H. When $0 < \alpha < \pi/2$, these fields are no longer isotropic. In this case, they are fractional Brownian fields whose non-null frequency components are restricted between frequency directions $-\alpha$ and α. As α decreases to 0, non-null field frequency components become more and more focused around the horizontal direction. In Figure 2, some elementary field realizations are shown for illustrating both the effect of increasing H on the field regularity and the effect of decreasing α on its anisotropy. For the evaluation, we considered elementary fields of varying degrees of

regularity and anisotropy, taking all parameter pairs (H, α) for H in $\{0.2, 0.5, 0.8\}$ and α in $\{\pi/3, \pi/2\}$.

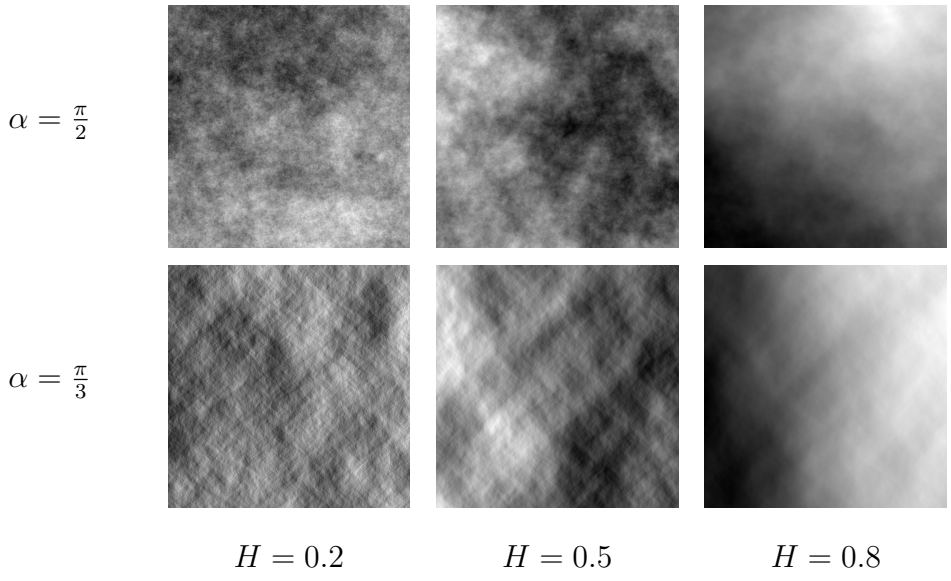

FIGURE 2. Realizations on $[0,1]^2$ of elementary fields obtained for different values of H and α using the TBM with 5900 bands.

Let us further mention that the semi-variograms of elementary fields can be computed using the closed form given in Appendix A (Supplementary materials, Proposition 1, Equation (1)). As will become apparent below, this is of particular interest for the computation of evaluation criteria. In Figure 3, some of these semi-variograms are presented for different degrees of regularity and anisotropy.

Finally, let us notice that any anisotropic fractional Brownian field whose spectral density is defined with piecewise constant functions h and c can be decomposed as a sum of independent elementary fields. Hence, although achieved on elementary fields, our evaluation accounts for more general anisotropic fractional Brownian fields.

4.2. **Approximation error.** As mentionned in Section 2.3, simulation errors result from the distance separating simulation and theoretical fields. This distance can be defined as the Kolmogorov distance between distributions of theoretical and simulation fields at each position x. As stated in Theorem 2.2 (Equation (13)), the Kolmogorov distance

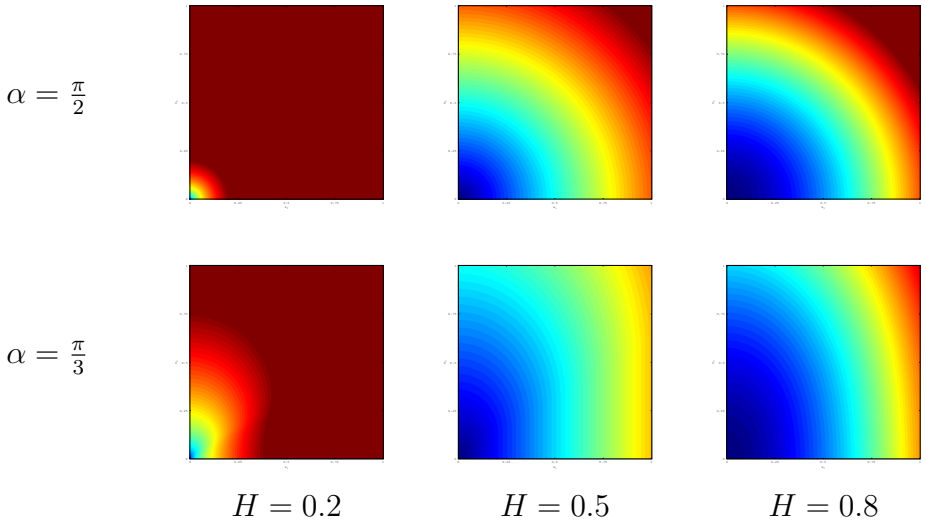

FIGURE 3. Semi-variograms on $[0,1]^2$ of elementary fields for different values of H and α.

is further bounded by $d_{\Theta,\Lambda}(x) = \frac{|v_X(x) - v_{\Theta,\Lambda}(x)|}{v_X(x)}$, which is proportional to the error made when approximating the semi-variogram of X by that of $X_{\Theta,\Lambda}$. Moreover, when X is an elementary field, it is possible to compute the bound $d_{\Theta,\Lambda}(x)$ using closed forms of $v_{\Theta,\Lambda}(x)$ and $v_X(x)$ given by Equation (10) and Appendix A (Proposition 1, Equation (1)), respectively. Hence, using elementary fields, we could numerically evaluate a simulation error by averaging values of $d_{\Theta,\Lambda}(x)$ over points x of a uniform subgrid of $[0,1]^2$:

$$d_{\Theta,\Lambda} = \sum_{1 \le k,l \le p} d_{\Theta,\Lambda}\left(\frac{k}{p}, \frac{l}{p}\right) = \sum_{1 \le k,l \le p} \frac{|v_X(\frac{k}{p}, \frac{l}{p}) - v_{\Theta,\Lambda}(\frac{k}{p}, \frac{l}{p})|}{v_X(\frac{k}{p}, \frac{l}{p})},$$

with $p = 64$. As evidenced by Equation (15), the measured error $d_{\Theta,\Lambda}$ depends on the precision parameter ε_Θ of the simulation field. Figure 4 illustrates the effect of increasing ε_Θ (*i.e.* reducing the simulation precision) on simulations of a fractional Brownian field of Hurst index $H = 0.2$. When the precision becomes too low ($\varepsilon_\Theta \ge 0.25$), field realizations exhibit some stripes in different directions, and the semi-variograms of the simulation fields present some singularities on lines radiating from the origin. This well-known effect, often called artifact banding in the literature (Gneiting, 1998; Mantoglou and Wilson, 1982; Emery and Lantuéjoul, 2006; Emery, 2008), is due to the fact that the contribution of a

band process Y_i to the sum defining the simulation field (see Equation (9)) is null on the line orthogonal to the band direction θ_i and passing through the origin.

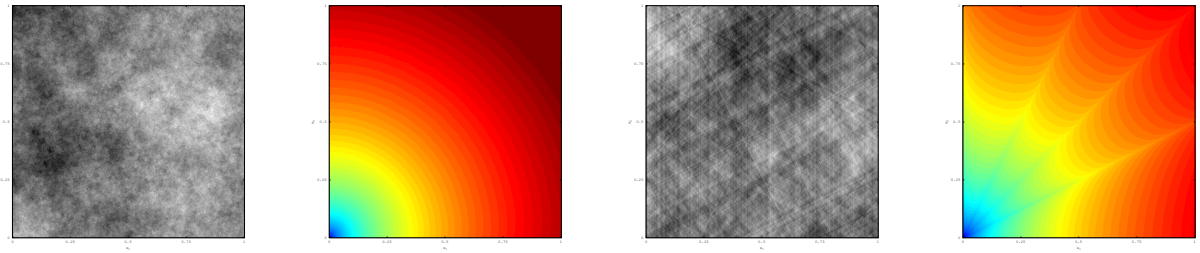

FIGURE 4. Effect of reducing the field precision on simulations of a fractional Brownian field of Hurst index $H = 0.2$.

In Figure 5, we plotted values of error bounds $d_{\Theta,\Lambda}$ obtained for different elementary fields as a function of the precision parameter ε_Θ. Whatever the field parameters, error bounds varied almost linearly with respect to ε_Θ. They did not seem to depend on the regularity parameter H. However, they were slightly dependent on the anisotropy parameter α, especially at low precision ($\varepsilon_\Theta > 0.03$). Error bounds of all fields fell below 1% when $\varepsilon_\Theta < 0.02$, such a precision being reached with around 150 simulation bands.

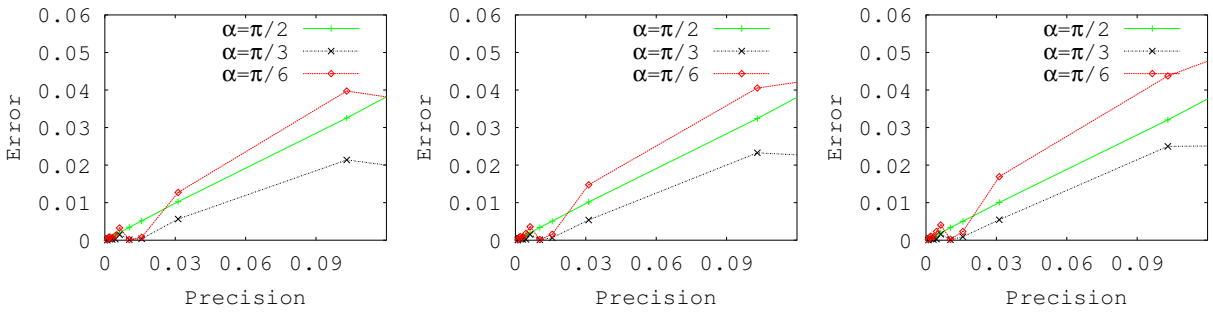

FIGURE 5. Variations of the error bound $d_{\Theta,\Lambda}$ relative to the precision parameter ε_Θ for elementary fields with different values of H and α.

4.3. **Estimation error.** We also conducted numerical experiments to evaluate errors that arise when estimating field features (*e.g.* parameters, semi-variograms) from field simulations. Applying the TBM (with 1321 bands on a 64×64 grid of $[0,1]^2$), we simulated 2000 independent realizations $\{y^{(k)}, k=1,\cdots,2000\}$ of a given elementary field X of semi-variogram v_X. Given $k\in\{1,\cdots,2000\}$, we then computed the empirical semi-variogram $v^{(K)}(x)$ at position x using the K first samples $v^{(K)}(x) = \frac{1}{2K}\sum_{k=1}^{K}(y^{(k)}(x))^2$. Finally, we computed an estimation error $d^{(K)}(x) = \frac{|v_X(x)-v^{(K)}(x)|}{v_X(x)}$ at point x, and its average over points x of the grid $d^{(K)} = \sum_{1\le k,l\le p} d^{(K)}\left(\frac{k}{p},\frac{l}{p}\right) = \sum_{1\le k,l\le p}\frac{|v_X(\frac{k}{p},\frac{l}{p})-v^{(K)}(\frac{k}{p},\frac{l}{p})|}{v_X(\frac{k}{p},\frac{l}{p})}$, with $p=64$.

In Figure 6, we plotted the estimation error $d^{(K)}$ as a function of the sample number K for different elementary fields. For a fixed value of the regularity parameter H, the convergence of the error to zero is about the same for all values of the anisotropy parameter α. However, the convergence gets slower and slower as H increases. In all cases, around 1000 samples are required for the error to get below 5%.

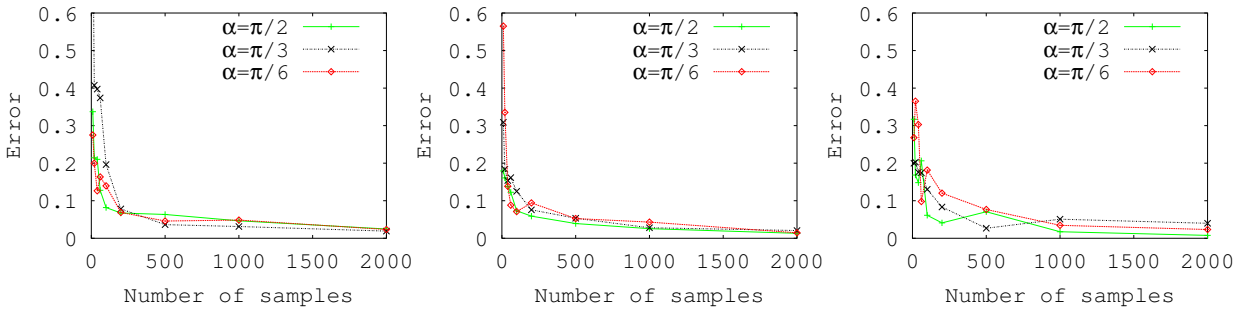

$H=0.2$ $H=0.5$ $H=0.8$

FIGURE 6. Variations of the estimation error relative to the number K of samples for elementary fields with different values of H and α.

In addition to their accuracy, the simulated fields have interesting statistical properties. Like the AFBF, they are Gaussian and have stationary increments by construction. Moreover, they share self-similar properties with the AFBF. In particular, for a FBF of Hurst index H, the logarithm of quadratic variations is asymptotically linked to the logarithm of the scale by a linear relationship of slope $2H$ (Biermé and Richard, 2008; Richard and

Biermé, 2010). As illustrated in Figure 7 (a), such an asymptotic property could be observed for TBM simulations of FBF. In this experiment, the coefficient of determination (R^2) for the linear regression of the variations with respect to scale was about 0.98 on average over 40 simulations (with a standard deviation of 0.07).

As a comparison, we conducted the same experiment using a spectral simulation method (Biermé and Richard, 2008). This method is based on an approximation of the stochastic integral of the harmonizable representation of the field, which is computed with a discrete Fourier transform. In order to mitigate the effects of the discretization (in both space and frequency domains), two integer oversampling factors are used: α, an oversampling rate, and β, a domain extension factor. Thus, the spectral simulation of the field on the domain $[0,1)^2 \cap r^{-1}\mathbb{Z}^2$ is obtained by cropping and subsampling a larger field simulated on the domain $[0,\beta)^2 \cap (\alpha r)^{-1}\mathbb{Z}^2$. The larger α and β, the more accurate the spectral method is (more precisely, α permits capturing the high-frequency content of the field, while β aims at avoiding the undesired periodization effect of the discrete Fourier transform), but this accuracy has a cost, since a 2D discrete Fourier transform has to be performed on an image of size $(\alpha\beta r)^2$. In experiments, we used $\alpha = \beta = 2$ for $r = 600$, so that the spectral simulation takes about the same time as the TBM with 400 bands (15s using our Matlab implementation). In Figure 7, notice that relationships between variations and scales obtained for the spectral method (right) are not as linear as for the TBM (left). This suggests that spectral simulations lack self-similarity, and are not as truthful to the model as the TBM ones. Moreover, on spectral simulations the relationships between variations and scales significantly depart from the theoretical ones. In particular, the slope of lines obtained by linear regressions of variations on the smallest scales is larger than expected; on average, it is 0.54 instead of 0.4. This is in sharp contrast with the TBM simulations for which the mean slope is close to 0.4. But, the slope is directly related to the field regularity (Biermé and Richard, 2008; Richard and Biermé, 2010). Hence, whereas the regularity of TBM simulations corresponds to that of the model, the one for spectral simulations is higher. This drawback of the spectral method mainly results from cutting

field high-frequencies when approximating its integral representation. Considering larger values of α and β would improve the accuracy of the spectral method, but the cost in time and memory would become rapidly prohibitive. Thus, the TBM appears superior to the spectral method for simulating accurately fields on a large grid.

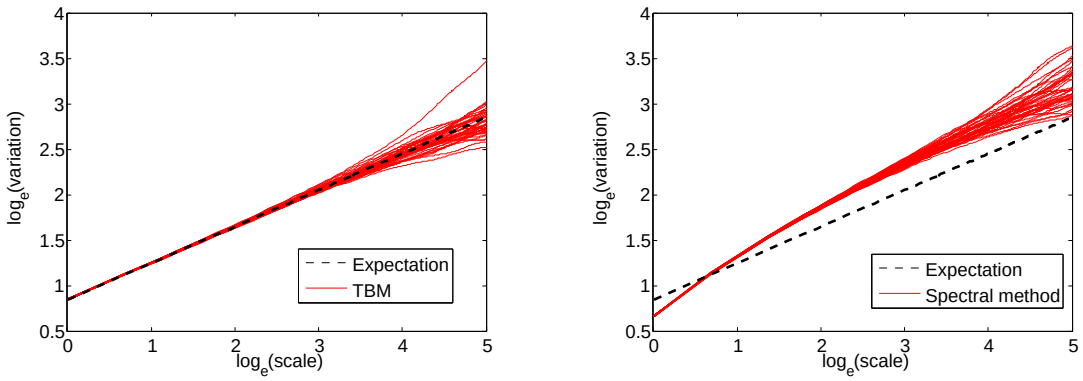

FIGURE 7. Quadratic variations computed on 40 realizations of size 600×600 of a FBF of Hurst index 0.2 obtained using the TBM with 400 bands (left) and the spectral method with oversampling factors $\alpha = \beta = 2$ (right).

5. Applications

In this section, we describe some applications of the proposed simulation method.

5.1. **Visualization of anisotropic fields associated with different topothesy functions.** In Figure 2, some elementary fields were displayed. However, simulation possibilities offered by the TBM go far beyond those fields, as there is a large choice of parameter definitions and tunings. Using the TBM, it becomes possible to visualize truthful realizations of different anisotropic field models studied in the literature (Bonami and Estrade, 2003; Biermé *et al.*, 2011; Davies and Hall, 1999; Richard and Biermé, 2010). In the generic model defined by Equation (5), we recall that the field anisotropy is introduced through two direction-dependent and π-periodic functions: the Hurst function h and the topothesy function c. So as to illustrate the effect of varying these parameter functions, we set $0 < \mu_1 \leq \mu_2 < 1$ and considered two functions of different regularity:

- a discontinuous function $g_1(\theta) = \begin{cases} \mu_1 & \text{if } \theta \in (-\frac{\pi}{4}, \frac{\pi}{4}) \text{ modulo } \pi, \\ \mu_2 & \text{otherwise.} \end{cases}$
- an infinitely differentiable function $g_2(\theta) = \mu_2 - (\mu_2 - \mu_1)\cos^2\theta$.

Fixing the topothesy function to a constant ($c \equiv 1$), we first simulated field realizations with Hurst functions $h = g_i$ for $i = 1, 2$ and different pairs of parameter values (μ_1, μ_2); results are shown in Figure 8. In these realizations, the degree of anisotropy can be measured as the difference $\mu_2 - \mu_1$ between maximal and minimal Hurst indices. It is the same for realizations of the first and second columns ($\mu_2 - \mu_1 = 0.3$), and higher for those of the third column ($\mu_2 - \mu_1 = 0.6$). Moreover, the Hölder regularity of those realizations is equal to μ_1. It is the same for realizations of the first and third columns ($\mu = 0.2$) and higher for those of the second column ($\mu = 0.5$). Comparing realizations in a same row, we clearly see the effect of anisotropy and regularity variations on field textures: as the field regularity decreases, the texture gets rougher, and, as the field anisotropy increases, texture patterns get more obviously oriented. Besides, comparing realizations in a same column, we can observe texture differences induced by changing the regularity of the Hurst function h in the model. Realizations obtained with a discontinuous function h (in the first row) have some linear patterns which are not present on those obtained with a more regular function h (second row).

Fixing the Hurst function to a constant ($h \equiv 0.5$), we also simulated field realizations with topothesy functions $c = g_i$ for $i = 1, 2$ and different pairs of parameter values (μ_1, μ_2). Some visual differences can be clearly distinguished in Figure 9, in particular between the two images of column 3 (influence of the regularity of the topothesy function) and between the columns 1 and 3 (influence of the variations of the topothesy function).

5.2. **Irregular grids.** In the simulations we presented, field realizations were generated on a regular subgrid of $[0, 1]^2$. Using our TBM approach, it is however possible to simulate fields on non-uniformly spaced positions. To do so, the only condition is that the position coordinates are all rational; this is required for the exact simulation of FBM on turning

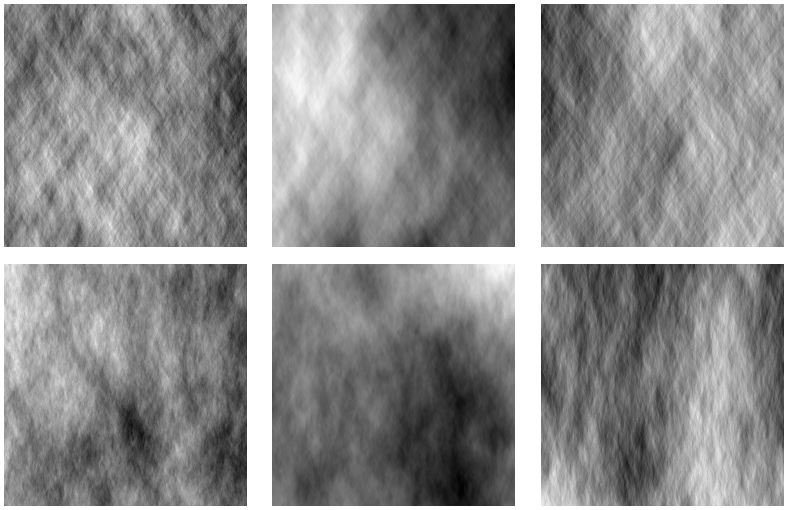

FIGURE 8. Field realizations obtained with different Hurst functions h. For all realizations, the topothesy function is $c \equiv 1$. In the first and second rows, Hurst functions are $h = g_1$ (discontinuous) and $h = g_2$ (infinitely differentiable), respectively. In the first, second and third columns, the Hurst functions are specified by the parameter pair values $(\mu_1, \mu_2) = (0.2, 0.5)$, $(\mu_1, \mu_2) = (0.5, 0.8)$, and $(\mu_1, \mu_2) = (0.2, 0.8)$, respectively.

bands (see Section 3). The pseudo-polar grid is an example of a set of points satisfying this simulation condition (Averbuch *et al.*, 2008a). Such a grid is of particular interest for computing a discrete Radon transform (Averbuch *et al.*, 2008b), as its points are uniformly spread on different lines radiating from the origin. But Radon transforms are one of the key features for the construction of parameter estimators for AFBF (Biermé and Richard, 2008; Richard and Biermé, 2010). Hence, those estimators could be better discretized and evaluated using simulations on a pseudo-polar grid.

5.3. **Field deformations.** Due to the ability of the TBM to simulate fields on quasi-arbitrary points, it also becomes possible to simulate field deformations. For instance, let A be the 2×2-matrix of an affine transform (with rational components) and $\tilde{X} = X \circ A$ the deformation of the random field X by the affine transform A. Realization of $\tilde{X}$ on a uniform grid G of $[0,1]^2$ can be obtained by applying the TBM to the simulation of

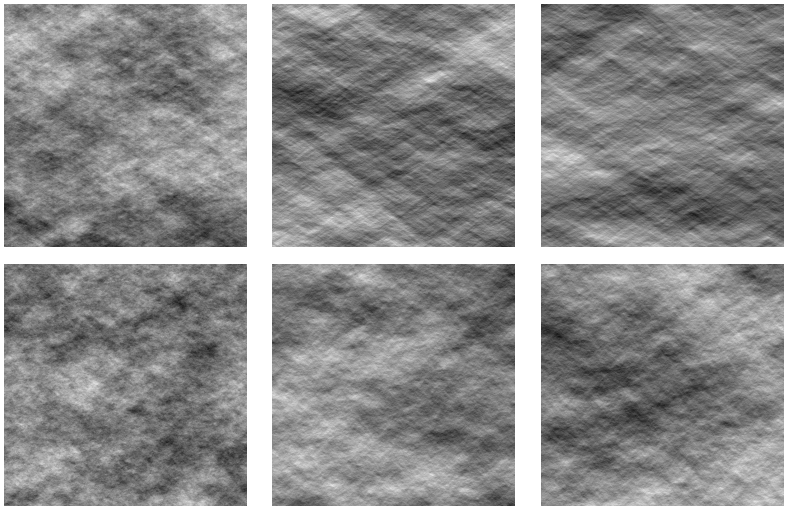

FIGURE 9. Field realizations obtained with different topothesy functions. For all realizations, the Hurst function is $h \equiv 0.2$. In the first and second rows, topothesy functions are $c = g_1$ (discontinuous) and $c = g_2$ (infinitely differentiable), respectively. In the first, second and third columns, the topothesy functions are specified by the parameter pair values $(\mu_1, \mu_2) = (1, 5)$, $(\mu_1, \mu_2) = (1, 100)$, and $(\mu_1, \mu_2) = (1, 1000)$, respectively.

X on $\{Ax, x \in G\}$. Figure 10 illustrates how an isotropic field can be deformed into an anisotropic field.

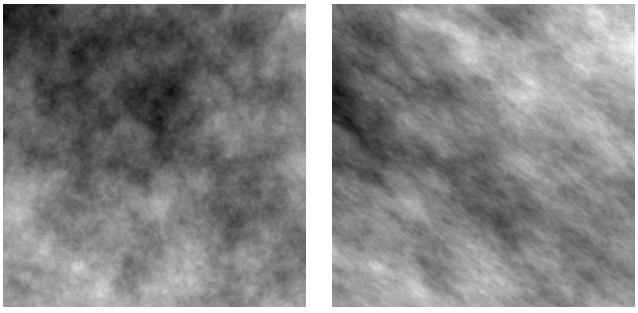

FIGURE 10. A simulated fractional Brownian field of Hurst index 0.5 (partially shown on the left), and its deformation by an horizontal shear transform (right).

6. Conclusion

We have constructed turning-band fields suited to the simulation of AFBF. This construction is based on the resolution of an integral equation specific to the non-stationary anisotropic context of AFBF. This ensures the convergence of simulation fields to target fields as the precision increases. Moreover, the band processes involved in the definition of simulation fields are simulated exactly using a circulant embedding method. Hence, errors produced by the simulation method are exclusively due to the approximation of the target field by the simulation field. This approximation error was evaluated theoretically and numerically. From a numerical point of view, we observed that it does not depend significantly on the regularity of target fields, nor on their degree of anisotropy. Experiments also suggest that simulations preserve the statistical properties of the target field. In the end, we obtained good simulation results with a relatively small number of bands (around 150 for images of size 600×600) at a low computational cost.

Supplementary Materials

The online supplementary materials consists in a single file (`supplementary.pdf`) that contains Appendix A (various technical results and proofs) and Appendix B (pseudo-code for the Dynamic Programming band selection algorithm).

Acknowledgements

This work is part of the research program MATAIM, supported by the Agence Nationale pour la Recherche (ANR-09-BLAN-0029-01).

References

Averbuch, A., Coifman, R., Donoho, D., Israeli, M., and Shkolnisky, Y. (2008a). A framework for discrete integral transformations I - the pseudo-polar Fourier transform. *SIAM J Sci Comput*, **30**(2), 764–784.

Averbuch, A., Coifman, R., Donoho, D., Israeli, M., Shkolnisky, Y., and Sedelnikov, I. (2008b). A framework for discrete integral transformations II - the 2D discrete Radon transform. *SIAM J Sci Comput*, **30**(2), 785–803.

Ayache, A., Bonami, A., and Estrade, A. (2005). Identification and series decomposition of anisotropic Gaussian fields. *Proc of the Catania ISAAC'05 congress*.

Bellman, R. (1954). The theory of dynamic programming. *Bull Amer Math Soc*, **60**, 503–515.

Biermé, H. and Richard, F.J.P. (2008). Estimation of anisotropic Gaussian fields through Radon transform. *ESAIM:P & S*, **12**(1), 30–50.

Biermé, H. and Richard, F.J.P. (2009). Anisotropic texture modeling and applications to medical image analysis, In *ESAIM Proc: Mathematical Methods for Imaging and Inverse Problems*, Volume 26, pages 100–122, Springer, H. Ammari (ed.).

Biermé, H. and Richard, F.J.P. (2011). Analysis of Texture Anisotropy Based on Some Gaussian Fields with Spectral Density, In *Springer Proc: Mathematical Image Processing*, pages 59–73, M. Bergounioux (ed.).

Biermé, H., Benhamou, C., and Richard, F.J.P. (2009). Parametric estimation for Gaussian operator scaling random fie lds and anisotropy analysis of bone radiograph textures. In K. Pohl, editor, *Proc. of the Int Conf on MICCAI*, pages 13–24, London, UK.

Biermé, H., Bonami, A., and José, L. (2011). Central limit theorems and quadratic variations in terms of spectral density. *Electron J Probab*, **16**(3), 362–395.

Bonami, A. and Estrade, A. (2003). Anisotropic analysis of some Gaussian models. *J Fourier Anal Appl*, **9**(3), 215–236.

Brooker, P. (1985). Two-dimensional simulation by turning bands. *Math Geol*, **17**(1), 81–90.

Brouste, A., Lambert-Lacroix, S., and J., Istas. (2007). On fractional Gaussian random fields simulations. *J Stat Softw*, **23**(1), 1–23.

Chan, G. (1999). An effective method for simulating Gaussian random fields. In *Proc of the statistical Computing section*, pages 133–138. Amerir. Statist.

Chilès, J. (1977). *Géostatique des phénomènes non stationnaires*. Ph.D. thesis, Univ Nancy.

Chilès, J. and Delfiner, P. (2012). *Geostatistics: modeling spatial uncertainty*. Wiley, New-York, 2nd Edition.

Christakos, G. (1987). Stochastic simulation of spatially correlated geo-processes. *Math Geol*, **19**(8), 807–831.

Davies, S. and Hall, P. (1999). Fractal analysis of surface roughness by using spatial data. *J R Stat Soc, Series B*, **61**, 3–37.

Dietrich, C. (1995). A simple and efficient space domain implementation of the turning bands method. *Water Resour Res*, **31**(1), 147–156.

Dietrich, C. and Newsam, G. (1997). Fast and exact simulation of stationary Gaussian processes through circulant embedding of the covariance matrix. *SIAM J Sci Comput*, **18**(4), 1088–1107.

Dimitrakopoulos, R. (1990). Conditional simulation of intrinsic random functions of order k. *Math Geol*, **22**(3), 361–380.

Emery, X. (2008). A turning bands program for conditional co-simulation of cross-correlated Gaussian random fields. *Comput Geosci*, **34**(12), 1850–1662.

Emery, X. and Lantuéjoul, C. (2006). TBSIM: A computer program for conditional simulation of three-dimensional Gaussian random fields via the turning bands method. *Comput Geosci*, **32**(10), 1615–1628.

Emery, X. and Lantuéjoul, C. (2008). A spectral approach to simulating intrinsic random fields with power and spline generalized covariances. *Comput Geosci*, **12**(1), 121–132.

Gneiting, T. (1996). Comment on "a simple and efficient space domain implementation of the turning bands method" by C. Dietrich. *Water Resour Res*, **32**(11), 3391–3396.

Gneiting, T. (1998). Closed form solutions of the two-dimensional turning bands equation. *Math Geol*, **30**(4), 379–390.

Journel, A. (1974). Geostatistics for conditional simulation of ore bodies. *Econ Geol*, **69**(5), 673–687.

Kolmogorov, A. N. (1940). Wienersche Spiralen und einige andere interessante Kurven in Hilbertsche Raum. *C. R. (Dokl.) Acad. Sci. URSS*, **26**, 115–118.

Lacaux, C. (2004). *Real Harmonizable Multifractional Lévy field*. Ph.D. thesis, Univ Toulouse.

Lantuéjoul, C. (2002). *Geostatistical Simulation: Models and Algorithms*. Springer.

Mandelbrot, B. B. and Van Ness, J. (1968). Fractional Brownian motion, fractionnal noises and applications. *SIAM Rev*, **10**, 422–437.

Mantoglou, A. (1987). Digital simulation of multivariate two- and three-dimensional stochastic processes with a spectral turning bands method. *Math Geol*, **19**(2), 129–149.

Mantoglou, A. and Wilson, J. (1982). The turning bands method for simulation of random fields using line generation by a spectral method. *Water Resour Res*, **18**(5), 1379–1394.

Matheron, G. (1973). The intrinsic random functions and their application. *Adv Appl Prob*, **5**, 439–468.

Pardo-Igúzquiza, E. and Chica-Olmo, M. (1993). The Fourier integral method: an efficient spectral method for simulation of random fields. *Math Geol*, **25**(2), 177–217.

Pardo-Igúzquiza, E. and Dowd, P. (2003). IRFK2D: a computer program for simulating intrinsic random functions of order k. *Comput Geosci*, **29**(6), 753–759.

Perrin, E., Harba, R., Jennane, R., and Iribarren, I. (2002). Fast and exact synthesis for 1-D fractional Brownian motion and fractional Gaussian noises. *IEEE Signal Process Lett*, **9**(11), 382–384.

Richard, F.J.P. and Biermé, H. (2010). Statistical tests of anisotropy for fractional Brownian textures. Application to full-field digital mammography. *J Math Imaging Vis*, **36**(3), 227–240.

Samorodnitsky, G. and Taqqu, M. S. (1994). *Stable non-Gaussian random processes*. Chapman & Hall, New York.

Saupe, D. (1988). Algorithms for random fractals, In *The science of fractal images*, Springer-Verlag, New-York, H.-O. Peitgen and D. Saupe (eds.).

Shinozuka, M. and Jan, C.-M. (1972). Digital simulation of random processes and its applications. *J Sound Vib*, **25**(1), 111 – 128.

Stein, M. L. (2002). Fast and exact simulation of fractional Brownian surfaces. *J Comput Graph Stat*, **11**(3), 587–599.

Wood, A. and Chan, G. (1994). Simulation of stationary Gaussian proceses on $[0,1]^d$. *J Comput Graph Stat*, **3**(4), 409–432.

Yin, Z. (1996). New methods for simulation of fractional Brownian motion. *J Comput Phys*, **127**(1), 66–72.

[1] LMA, CNRS UMR 7348, Université Poitiers, Téléport 2-BP30179, Boulevard Marie et Pierre Curie, 86962 Chasseneuil Cedex, France. *E-mail address*: hermine.bierme@math.univ-poitiers.fr

[2] Université Paris Descartes, MAP5, CNRS UMR 8145, Sorbonne Paris Cité, 45 rue des Saints-Pères, 75006 Paris, France. *E-mail address*: lionel.moisan@parisdescartes.fr

[3] Aix Marseille Université, CNRS, Centrale Marseille, I2M, UMR 7373, 13453 Marseille, France. *E-mail address*: frederic.richard@univ-amu.fr

SUPPLEMENTARY MATERIALS FOR THE PAPER:

A TURNING-BAND METHOD FOR THE SIMULATION OF ANISOTROPIC FRACTIONAL BROWNIAN FIELDS

HERMINE BIERMÉ [1], LIONEL MOISAN [2], AND FRÉDÉRIC RICHARD[3]

Appendix A: detailed results and proofs

1. Semi-variogram of an elementary field

Proposition 1. *Let $H \in (0,1)$ and $-\pi/2 \leq \alpha_1 < \alpha_2 \leq \pi/2$. Let denote v_{H,α_1,α_2} the semi-variogram of an AFBF with $h = H$ and $c = \mathbf{1}_{[\alpha_1,\alpha_2]}$. Then,*

$$\forall x \in \mathbb{R}^2,\ v_{H,\alpha_1,\alpha_2}(x) = 2^{2H-1}\gamma(H) C_{H,\alpha_1,\alpha_2}(\arg(x))|x|^{2H}, \tag{1}$$

where C_{H,α_1,α_2} is a π-periodic function defined on $(-\pi/2, \pi/2]$ by

$$C_{H,\alpha_1,\alpha_2}(\theta) = \begin{cases} \beta_H\left(\frac{1-\sin(\alpha_2-\theta)}{2}\right) + \beta_H\left(\frac{1-\sin(\alpha_1-\theta)}{2}\right) & \text{if} \quad \alpha_1 \leq \theta + \pi/2 \leq \alpha_2 \\ \beta_H\left(\frac{1+\sin(\alpha_2-\theta)}{2}\right) + \beta_H\left(\frac{1+\sin(\alpha_1-\theta)}{2}\right) & \text{if} \quad \alpha_1 \leq \theta - \pi/2 \leq \alpha_2 \\ \left|\beta_H\left(\frac{1-\sin(\alpha_2-\theta)}{2}\right) - \beta_H\left(\frac{1-\sin(\alpha_1-\theta)}{2}\right)\right| & \text{otherwise} \end{cases}$$

with β_H the incomplete Beta function given by

$$\forall t \in [0,1],\ \beta_H(t) = \int_0^t u^{H-1/2}(1-u)^{H-1/2} du,$$

and γ is defined by $\gamma(H) = \dfrac{\pi}{H\Gamma(2H)\sin(H\pi)}$.

Proof. According to Proposition 2.1 (main paper), for all $x \in \mathbb{R}^2$,

$$\begin{aligned} v_{H,\alpha_1,\alpha_2}(x) &= \frac{1}{2}\int_{-\pi/2}^{\pi/2} \gamma(h(\theta))c(\theta)|x \cdot u(\theta)|^{2h(\theta)} d\theta \\ &= \frac{1}{2}\gamma(H)|x|^{2H}\int_{\alpha_1}^{\alpha_2} |\cos(\theta - \arg(x))|^{2H} d\theta. \end{aligned}$$

We will use the following lemma.

Lemma 2. *Let $a, b \in \mathbb{R}$ with $-\pi/2 \leq a < b \leq \pi/2$, then*

$$\int_a^b |\cos(\theta)|^{2H} d\theta = 2^{2H} \left(\beta_{H} \left(\frac{1+\sin(b)}{2} \right) - \beta_{H} \left(\frac{1+\sin(a)}{2} \right) \right).$$

Proof. Since we assume that $-\pi/2 \leq a < b \leq \pi/2$,

$$\begin{aligned} \int_a^b |\cos(\theta)|^{2H} d\theta &= \int_a^b \left(1 - \sin(\theta)^2\right)^{H-1/2} \cos(\theta) d\theta \\ &= \int_{\sin(a)}^{\sin(b)} (1-u^2)^{H-1/2} du, \end{aligned}$$

by the change of variables $u = \sin(\theta)$. Then, by the change of variables $v = \frac{1+u}{2}$, we obtain

$$\int_a^b |\cos(\theta)|^{2H} d\theta = 2^{2H} \int_{\frac{1+\sin(a)}{2}}^{\frac{1+\sin(b)}{2}} (1-v)^{H-1/2} v^{H-1/2} dv,$$

which gives the result. □

This allows us to get the next result, which concludes the proof.

Corollary 3. *Let $a, b \in \mathbb{R}$ with $0 \leq b - a \leq \pi$, then*

$$\int_a^b |\cos(\theta)|^{2H} d\theta = 2^{2H} \begin{cases} \left| \beta_{H} \left(\frac{1+\sin(b)}{2} \right) - \beta_{H} \left(\frac{1+\sin(a)}{2} \right) \right| & \text{if} \quad (a,b) \cap \{\frac{\pi}{2} + \mathbb{Z}\pi\} = \emptyset \\ \beta_{H} \left(\frac{1+\sin(b)}{2} \right) + \beta_{H} \left(\frac{1+\sin(a)}{2} \right) & \text{if} \quad (a,b) \cap \{-\frac{\pi}{2} + 2\mathbb{Z}\pi\} \neq \emptyset \\ \beta_{H} \left(\frac{1-\sin(b)}{2} \right) + \beta_{H} \left(\frac{1-\sin(a)}{2} \right) & \text{if} \quad (a,b) \cap \{\frac{\pi}{2} + 2\mathbb{Z}\pi\} \neq \emptyset \end{cases}$$

Proof. We first assume that $(a,b) \cap \frac{\pi}{2} + \mathbb{Z}\pi = \emptyset$. Since $0 \leq b - a \leq \pi$, one can find $k \in \mathbb{Z}$ such that $-\pi/2 \leq a + k\pi < b + k\pi \leq \pi/2$. The result follows from Lemma 2 when k is even. When k is odd,

$$\int_a^b |\cos(\theta)|^{2H} d\theta = \int_{a+k\pi}^{b+k\pi} |\cos(\theta)|^{2H} d\theta = 2^{2H} \left(\beta_{H} \left(\frac{1-\sin(b)}{2} \right) - \beta_{H} \left(\frac{1-\sin(a)}{2} \right) \right),$$

according to Lemma 2. Note that by a change of variables, for all $\theta \in \mathbb{R}$

$$\beta_{H} \left(\frac{1-\sin(\theta)}{2} \right) = \beta_{H}(1) - \beta_{H} \left(\frac{1+\sin(\theta)}{2} \right) \tag{2}$$

and the result follows.

Now let assume that $-\frac{\pi}{2}+2\mathbb{Z}\pi \neq \emptyset$. Then, one can find $k \in \mathbb{Z}$ such that $a+2k\pi < -\pi/2 < b+2k\pi$, and according to Lemma 2,

$$\begin{aligned}
\int_a^b |\cos(\theta)|^{2H} d\theta &= \int_{a+2k\pi}^{b+2k\pi} |\cos(\theta)|^{2H} d\theta \\
&= \int_{a+2k\pi}^{-\pi/2} |\cos(\theta)|^{2H} d\theta + \int_{\pi/2}^{b+2k\pi} |\cos(\theta)|^{2H} d\theta \\
&= \int_{a+\pi+2k\pi}^{\pi/2} |\cos(\theta)|^{2H} d\theta + 2^{2H}\beta_{_H}\left(\frac{1+\sin(b)}{2}\right) \\
&= 2^{2H}\left(\beta_{_H}(1) - \beta_{_H}\left(\frac{1+\sin(a+\pi)}{2}\right) + \beta_{_H}\left(\frac{1+\sin(b)}{2}\right)\right),
\end{aligned}$$

which concludes this case using (2). The last case is similar. □

2. Proof of Theorem 2.2

Let us write $X_{\theta_i}(x) := Y_i(x \cdot u(\theta_i))$, for $x \in \mathbb{R}^2$, with Y_i a FBM of order $h(\theta_i)$. First, note that $X_{\theta_i}(0) = Y_i(0) = 0$ a.s. Moreover, since Y_i is a centered Gaussian random process it is clear that X_{θ_i} is a centered Gaussian random field on $\mathbb{R}^2$. Finally, since Y_i has stationary increments, for any $x_0 \in \mathbb{R}^2$, writing $t_{0,i} = x_0 \cdot u(\theta_i) \in \mathbb{R}$,

$$\begin{aligned}
\{X_{\theta_i}(x+x_0) - X_{\theta_i}(x_0); x \in \mathbb{R}^2\} &= \{Y_i(x \cdot u(\theta_i) + t_{0,i}) - Y_i(t_{0,i}); x \in \mathbb{R}^2\} \\
&\overset{fdd}{=} \{Y_i(x \cdot u(\theta_i)) - Y_i(0); x \in \mathbb{R}^2\}, \\
&= \{X_{\theta_i}(x) - X_{\theta_i}(0); x \in \mathbb{R}^2\}.
\end{aligned}$$

It follows that $X_{\Theta,\Lambda}$ is a centered Gaussian random field on $\mathbb{R}^2$ with stationary increments as it is a sum of independent centered Gaussian random fields on $\mathbb{R}^2$ with stationary increments. Since $X_{\Theta,\Lambda}(0) = 0$ a.s.,

$$\begin{aligned}
v_{X_{\Theta,\Lambda}}(x) &= \frac{1}{2}\mathbb{E}\left(X_{\Theta,\Lambda}(x)^2\right) = \frac{1}{2}\mathrm{Var}(X_{\Theta,\Lambda}(x)), \text{ since } X_{\Theta,\Lambda} \text{ is centered,} \\
&= \frac{1}{2}\sum_{i=1}^{n} \lambda_i \gamma(h(\theta_i)) c(\theta_i) \mathrm{Var}(Y_i(x \cdot u(\theta_i))), \text{ by independence,} \\
&= \frac{1}{2}\sum_{i=1}^{n} \lambda_i \gamma(h(\theta_i)) c(\theta_i) |x \cdot u(\theta_i)|^{2h(\theta_i)} = v_{\Theta,\Lambda}(x).
\end{aligned}$$

Let $N \sim \mathcal{N}(0,1)$, then for $x \neq 0$,

$$d_{Kol}(X_{\Theta,\Lambda}(x), X(x)) = d_{Kol}(\sqrt{v_{\Theta,\Lambda}(x)}N, \sqrt{v_X(x)}N).$$

Then Inequality (13) in Theorem 2.2 follows from the fact that $d_{Kol}(\sigma' N, \sigma N) \leq 2\frac{|\sigma^2-\sigma'^2|}{\sigma^2}$. Actually, there is nothing to prove when $\sigma = \sigma'$ or when $2\frac{|\sigma^2-\sigma'^2|}{\sigma^2} > 1$, so we can assume that $\sigma \neq \sigma'$ and $2\frac{|\sigma^2-\sigma'^2|}{\sigma^2} \leq 1$, which implies that $\left(\frac{\sigma}{\sigma'}\right)^2 \leq 2$. First, let us suppose that $\sigma'' := \sigma'/\sigma > 1$ so that $d_{Kol}(\sigma' N, \sigma N) = \sup_{z>0} \mathbb{P}(z \leq N \leq \sigma'' z)$, using the fact that $\sup_{t>0} |\mathbb{P}(N \leq \sigma' t) - \mathbb{P}(N \leq \sigma t)| = \sup_{z>0} \mathbb{P}(z < N \leq \sigma'' z)$, while, since $-N \overset{d}{=} N$, $\sup_{t<0} |\mathbb{P}(N \leq \sigma' t) - \mathbb{P}(N \leq \sigma t)| = \sup_{z>0} \mathbb{P}(z \leq N < \sigma'' z)$. But, for $\sigma'' > 1$ and $z > 0$, we get $\mathbb{P}(z < N \leq \sigma'' z) \leq (\sigma'' - 1) z e^{-z^2/2} \leq \sigma''^2 - 1 = \frac{\sigma'^2-\sigma^2}{\sigma^2}$. In the remaining case $\sigma'' := \sigma'/\sigma < 1$, one has $d_{Kol}(\sigma' N, \sigma N) \leq \frac{\sigma^2-\sigma'^2}{\sigma'^2} \leq 2\frac{|\sigma^2-\sigma'^2|}{\sigma^2}$, using the fact that $\left(\frac{\sigma}{\sigma'}\right)^2 \leq 2$.

For the second part of the proof, we have a sequence (Θ_n, Λ_n) such that $v_{\Theta_n,\Lambda_n}(x) \underset{n\to+\infty}{\longrightarrow} v_X(x)$ for all $x \in \mathbb{R}^2$. By stationarity of the increments, for all $n \geq 1$, for all $x, y \in \mathbb{R}^2$,

$$\mathrm{Cov}(X_{\Theta_n,\Lambda_n}(x), X_{\Theta_n,\Lambda_n}(y)) = v_{\Theta_n,\Lambda_n}(x) + v_{\Theta_n,\Lambda_n}(y) - v_{\Theta_n,\Lambda_n}(x-y),$$

and similarly for $\mathrm{Cov}(X(x), X(y))$ and v_X. It follows that $\mathrm{Cov}(X_{\Theta_n,\Lambda_n}(x), X_{\Theta_n,\Lambda_n}(y))$ tends to $\mathrm{Cov}(X(x), X(y))$ for all $x, y \in \mathbb{R}^2$. Using a Cramér-Wold device, this implies that the field $(X_{\Theta_n,\Lambda_n}(x))_{x\in\mathbb{R}^2}$ converges to $(X(x))_{x\in\mathbb{R}^2}$ in the sense of finite dimensional distributions.

3. Approximation error for an elementary field

Proposition 4. *Let c and h be two π-periodic measurable functions defined on $(-\pi/2, \pi/2]$ by $h = H$ for some $H \in (0,1)$ and $c = \mathbf{1}_{[\alpha_1,\alpha_2]}$ for $-\pi/2 \leq \alpha_1 < \alpha_2 \leq \pi/2$. Let $\Theta = (\theta_i)_{1\leq i\leq n}$ with $\alpha_1 \leq \theta_1 < \ldots < \theta_n \leq \alpha_2$ and $\theta_0 = \alpha_1$, $\theta_{n+1} = \alpha_2$. Choose Λ as $\lambda_1 = \theta_2 - \theta_0$ and $\lambda_i = \theta_{i+1} - \theta_i$ for $2 \leq i \leq n$. Then, one can find a positive constant $C > 0$, independent of Θ, Λ, such that for all $x \in \mathbb{R}^2$,*

$$d_{Kol}(X_{\Theta,\Lambda}(x), X_{H,\alpha_1,\alpha_2}(x)) \leq C\varepsilon_\Theta^{\min(2H,1)}, \tag{3}$$

where the precision parameter ε_Θ *is defined by* $\varepsilon_\Theta = \max_{i=1,\cdots,n+1}(\theta_i - \theta_{i-1})$ *(see Equation (11) in the main paper).*

Moreover, when choosing $\lambda_1 = (\theta_1 - \theta_0) + \frac{\theta_2 - \theta_1}{2}, \lambda_n = (\theta_{n+1} - \theta_n) + \frac{\theta_n - \theta_{n-1}}{2}$ *and* $\lambda_i = \frac{\theta_{i+1} - \theta_{i-1}}{2}$ *for* $2 \leq i \leq n-1$*, one can find a positive constant* $C > 0$*, independent of* Θ, Λ*, such that for all* $x \in \mathbb{R}^2$*,*

$$d_{Kol}(X_{\Theta,\Lambda}(x), X_{H,\alpha_1,\alpha_2}(x)) \leq C \begin{cases} \varepsilon_\Theta^3 \delta_\Theta^{-2+\min(2H,1)} + \varepsilon_\Theta^{1+\min(2H,1)} & \text{if } H \neq 1/2, \\ \varepsilon_\Theta^3 \delta_\Theta^{-1} |\log(\delta_\Theta)| + \varepsilon_\Theta^2 & \text{if } H = 1/2 \end{cases} \tag{4}$$

with $\delta_\Theta = \min_{1 \leq i \leq n-1}(\theta_{i+1} - \theta_i)$.

Proof. Note that $X_{\Theta,\Lambda}(0) = X_{H,\alpha_1,\alpha_2}(0) = 0$ a.s. so that $d_{Kol}(X_{\Theta,\Lambda}(0), X_{H,\alpha_1,\alpha_2}(0)) = 0$. Let $x \in \mathbb{R}^2$ with $x \neq 0$. Then, the error of approximation is bounded by

$$\frac{v_{H,\alpha_1,\alpha_2}(x) - v_{\Theta,\Lambda}(x)}{v_{H,\alpha_1,\alpha_2}(x)},$$

with $v_{H,\alpha_1,\alpha_2}(x) = \frac{1}{2}\gamma(H)|x|^{2H} \int_{\alpha_1}^{\alpha_2} |\cos(\theta - \arg(x))|^{2H} d\theta$ and

$$v_{\Theta,\Lambda}(x) = \frac{1}{2}\gamma(H)|x|^{2H} \sum_{i=1}^{n} \lambda_i |\cos(\theta_i - \arg(x))|^{2H}.$$

First let us remark that, since $\theta' \mapsto |\cos(\theta - \theta')|^{2H}$ is continuous, non-negative and not identically equal to 0, one can find $c_1 > 0$ such that $\int_{\alpha_1}^{\alpha_2} |\cos(\theta - \arg(x))|^{2H} d\theta \geq c_1$ for all $x \in \mathbb{R}^2$. It follows that

$$d_{Kol}(X_{\Theta,\Lambda}(x), X_{H,\alpha_1,\alpha_2}(x)) \leq c_1^{-1} \left(\int_{\alpha_1}^{\alpha_2} |\cos(\theta - \arg(x))|^{2H} d\theta - \sum_{i=1}^{n} \lambda_i |\cos(\theta_i - \arg(x))|^{2H} \right).$$

Now, let us write

$$g_x(\theta) = |\cos(\theta - \arg(x))|^{2H}, \tag{5}$$

and note that

$$|g_x(\theta) - g_x(\theta')| \leq 2|\theta - \theta'|^{\min(2H,1)} \text{ for all } \theta, \theta' \in \mathbb{R}, \tag{6}$$

using the fact that $||t|^{2H} - |t'|^{2H}| \leq 2|t-t'|^{\min(2H,1)}$ for all $t, t' \in [-1,1]$. It follows that there exists $c_2 > 0$ such that for $0 \leq i \leq n$,

$$\left| \int_{\theta_i}^{\theta_{i+1}} (g_x(\theta) - g_x(\theta_i))\, d\theta \right| \leq c_2 (\theta_{i+1} - \theta_i)^{1+\min(1,2H)}. \tag{7}$$

Then, choosing $\lambda_1 = \theta_2 - \theta_0$ and $\lambda_i = \theta_{i+1} - \theta_i$ for $2 \leq i \leq n$, one has

$$\left| \int_{\alpha_1}^{\alpha_2} g_x(\theta) - \sum_{i=1}^{n} \lambda_i g_x(\theta_i) \right| \leq c_2 (\alpha_2 - \alpha_1) \max_{0 \leq i \leq n} (\theta_{i+1} - \theta_i)^{\min(1,2H)}.$$

Moreover g_x is of class $\mathcal{C}^2$ on $\mathbb{R} \setminus \{\arg(x) - \pi/2 + \pi\mathbb{Z}\}$ with

$$|g_x''(\theta)| \leq c_3 |\cos(\theta - \arg(x))|^{2H-2}, \text{ for all } \theta \notin \arg(x) - \pi/2 + \pi\mathbb{Z}, \tag{8}$$

for some $c_3 > 0$ (not depending on x). According to the trapezoidal rule, when $[\theta_i, \theta_{i+1}] \cap \{\arg(x) - \pi/2 + \pi\mathbb{Z}\} = \emptyset$,

$$\left| \int_{\theta_i}^{\theta_{i+1}} \left(g_x(\theta) - \frac{g_x(\theta_i) + g_x(\theta_{i+1})}{2} \right) d\theta \right| \leq \sup_{\theta \in [\theta_i, \theta_{i+1}]} |g_x''(\theta)| \frac{(\theta_{i+1} - \theta_i)^3}{12}. \tag{9}$$

Note also that using (6) one always has

$$\left| \int_{\theta_i}^{\theta_{i+1}} \left(g_x(\theta) - \frac{g_x(\theta_i) + g_x(\theta_{i+1})}{2} \right) d\theta \right| \leq c_2 (\theta_{i+1} - \theta_i)^{1+\min(1,2H)}. \tag{10}$$

For the sake of simplicity let us consider the case where $\arg(x) = \pi/2$ such that $-\pi/2 \leq \alpha_1 \leq \theta - \arg(x) + \pi/2 \leq \alpha_2 \leq \pi/2$ and

$$|\cos(\theta - \arg(x))| \geq \frac{2}{\pi} |\theta - \arg(x) + \pi/2| = \frac{2}{\pi} |\theta|.$$

If $\theta_{n+1} \leq 0$ we set $m = n+1$, if $\theta_0 > 0$ we set $m = 0$ and otherwise we choose $m \in \{0, \ldots, n\}$ such that $\theta_m \leq 0 < \theta_{m+1}$. Then, according to (8), since $2H - 2 < 0$, for $i > m+2$,

$$\sup_{\theta \in [\theta_i, \theta_{i+1}]} |g_x''(\theta)| \leq c_3 \left(\frac{2}{\pi} \right)^{2H-2} \theta_i^{2H-2} \leq c_3 \left(\frac{2}{\pi} \right)^{2H-2} \frac{1}{\theta_{i-1} - \theta_i} \int_{\theta_{i-1}}^{\theta_i} \theta^{2H-2} d\theta,$$

with, when $m < n-3$,

$$\sum_{i=m+3}^{n-1} \int_{\theta_{i-1}}^{\theta_i} \theta^{2H-2} d\theta = \int_{\theta_{m+2}}^{\theta_n} \theta^{2H-2} d\theta \leq c_4 \begin{cases} (\theta_{m+2} - \theta_{m+1})^{-1+\min(2H,1)} & \text{if } H \neq 1/2 \\ |\log(\theta_{m+2} - \theta_{m+1})| & \text{if } H = 1/2 \end{cases}, \tag{11}$$

for some constants $c_3, c_4 > 0$. While for $i < m-1$ one has

$$\sup_{\theta\in[\theta_i,\theta_{i+1}]} |{g_x}''(\theta)| \leq c_3 \left(\frac{2}{\pi}\right)^{2H-2} \frac{1}{\theta_{i+2}-\theta_{i+1}} \int_{\theta_{i+1}}^{\theta_{i+2}} |\theta|^{2H-2} d\theta,$$

with, when $m > 3$,

(12)

$$\sum_{i=1}^{m-2} \int_{\theta_{i-1}}^{\theta_i} \theta^{2H-2} d\theta = \int_{\theta_0}^{\theta_{m-2}} \theta^{2H-2} d\theta \leq c_5 \begin{cases} (\theta_{m-1}-\theta_{m-2})^{-1+\min(2H,1)} & \text{if } H \neq 1/2 \\ |\log(\theta_{m-1}-\theta_{m-2})| & \text{if } H = 1/2 \end{cases},$$

for some constant $c_5 > 0$. Let us choose $\lambda_1 = (\theta_1 - \theta_0) + \frac{\theta_2-\theta_1}{2}$, $\lambda_n = (\theta_{n+1}-\theta_n) + \frac{\theta_n-\theta_{n-1}}{2}$ and $\lambda_i = \frac{\theta_{i+1}-\theta_{i-1}}{2}$ for $2 \leq i \leq n-1$. Then, let us note that for $2 \leq i \leq n-1$ one has $\lambda_i = \frac{\theta_{i+1}-\theta_i}{2} + \frac{\theta_i-\theta_{i-1}}{2}$. Therefore

$$\begin{aligned} \sum_{i=2}^{n-1} \lambda_i g_x(\theta_i) &= \sum_{i=2}^{n-1} \frac{\theta_{i+1}-\theta_i}{2} g_x(\theta_i) + \sum_{i=1}^{n-2} \frac{\theta_{i+1}-\theta_i}{2} g_x(\theta_{i+1}) \\ &= \sum_{i=2}^{n-2} (\theta_{i+1}-\theta_i) \frac{g_x(\theta_i)+g_x(\theta_{i+1})}{2} + \frac{\theta_n-\theta_{n-1}}{2} g_x(\theta_{n-1}) + \frac{\theta_2-\theta_1}{2} g_x(\theta_2). \end{aligned}$$

It follows that

$$\begin{aligned} \sum_{i=1}^{n} \lambda_i g_x(\theta_i) &= \sum_{i=1}^{n-1} (\theta_{i+1}-\theta_i) \frac{g_x(\theta_i)+g_x(\theta_{i+1})}{2} + (\theta_1-\theta_0) g_x(\theta_1) + (\theta_{n+1}-\theta_n) g_x(\theta_n) \\ &= \sum_{i=1}^{n-1} \int_{\theta_i}^{\theta_{i+1}} \frac{g_x(\theta_i)+g_x(\theta_{i+1})}{2} d\theta + \int_{\theta_0}^{\theta_1} g_x(\theta_1) d\theta + \int_{\theta_n}^{\theta_{n+1}} g_x(\theta_n) d\theta. \end{aligned}$$

Then,

$$\begin{aligned} & \left| \int_{\alpha_1}^{\alpha_2} g_x(\theta) - \sum_{i=1}^{n} \lambda_i g_x(\theta_i) \right| \\ \leq & \sum_{i=1}^{n-1} \left| \int_{\theta_i}^{\theta_{i+1}} g_x(\theta) - \frac{g_x(\theta_i)+g_x(\theta_{i+1})}{2} d\theta \right| + \left| \int_{\theta_0}^{\theta_1} g_x(\theta) - g_x(\theta_1) d\theta \right| + \left| \int_{\theta_n}^{\theta_{n+1}} g_x(\theta) - g_x(\theta_n) d\theta \right| \\ \leq & \sum_{i=1}^{m-2} + \sum_{i=m+3}^{n-1} + \sum_{i=m-1}^{m+2} + \left| \int_{\theta_0}^{\theta_1} g_x(\theta) - g_x(\theta_1) d\theta \right| + \left| \int_{\theta_n}^{\theta_{n+1}} g_x(\theta) - g_x(\theta_n) d\theta \right|, \end{aligned}$$

which gives the result using (9) with (11) and (12) for the two first sums and using (7) and (10) for the other terms. The general case where $\arg(x) \neq \pi/2$ can be computed similarly. □

4. Proof of Proposition 2.3

The proof is similar to the proof of Proposition 4, considering

$$\tilde{g_x}(\theta) = \gamma(h(\theta))c(\theta)|x \cdot u(\theta))|^{2h(\theta)} = \gamma(h(\theta))c(\theta)|x|^{2h(\theta)}|\cos(\theta - \arg(x))|^{2h(\theta)}.$$

instead of $g_x(\theta)$ given by (5). Note that when h and c are assumed of class $\mathcal{C}^l$ ($l = 1$ or 2) on $[\alpha_1, \alpha_2] \subset [-\pi/2, \pi/2]$, one can find $C > 0$ such that for all $x \in T$,

$$|\tilde{g_x}(\theta) - \tilde{g_x}(\theta')| \leq C|\theta - \theta'|^{\min(2H(\alpha_1,\alpha_2),1)}, \text{ for all } \theta, \theta' \in [\alpha_1, \alpha_2],$$

and when $l = 2$,

$$|\tilde{g_x}''(\theta)| \leq C|\cos(\theta - \arg(x))|^{2H(\alpha_1,\alpha_2)-2}, \text{ for all } \theta \in [\alpha_1, \alpha_2] \text{ with } \theta \notin \arg(x) - \pi/2 + \pi\mathbb{Z},$$

where $H(\alpha_1, \alpha_2) = \min_{\theta\in[\alpha_1,\alpha_2]} h(\theta)$. These estimates allow us to proceed as in the proof of Proposition 4. The result follows by summing the integrals over which the functions h and c are regular using the fact that $H \leq H(\alpha_1, \alpha_2)$ for all α_1, α_2.

5. Simulation of a 1D FBM

Several methods for the synthesis of a 1D FBM have been proposed in the literature. Most of them are approximate procedures. However, considering equispaced points on the band, one can get exact simulations using the circulant embedding method as in Dietrich and Newsam (1997). Let us briefly recall this procedure. Let B_H be a FBM (with $H \in (0, 1)$) and $Z_H = (B_H(t + 1) - B_H(t))_{t\in\mathbb{R}}$ the associated fractional Gaussian noise, which is a stationary process with covariance function given by $\mathrm{Cov}(Z_H(t), Z_H(s)) = r_H(|t - s|)$ with $r_H(t) = \frac{1}{2}(|t+1|^{2H} - 2|t|^{2H} + |t-1|^{2H})$. For any $l \geq 1$, $(Z_H(0), \ldots, Z_H(l))$ is a centered Gaussian vector of size $l + 1$ with Toeplitz covariance matrix $R_H(l) = (r_H(|i - j|))_{0\leq i,j\leq l}$. One can embed $R_H(l)$ in a circulant matrix of size $2l$ given by $S_H(l) = \mathrm{circ}(s_H(l))$ with $s_H(l) = (r_H(0), \ldots r_H(l)\, r_H(l-1), \ldots r_H(1))$. The main interesting property of circulant matrices is that they are diagonalized in the discrete Fourier basis, with their eigenvalues given by the Discrete Fourier Transform of their first row. In particular one has $S_H(l) = \frac{1}{2l}F_{2l}^{*}\mathrm{diag}(F_{2l}s_H(l))F_{2l}$, where $F_{2l} = (e^{\frac{i\pi jk}{l}})_{0\leq i,j\leq 2l-1}$.

The main result of Perrin *et al.* (2002) is that for all $H \in (0,1)$ and $l \geq 1$, $F_{2l} s_H(l)$ always has positive entries, so that $S_H(l)$ is a covariance matrix. Moreover, if $\varepsilon_{2l}^{(1)}$ and $\varepsilon_{2l}^{(2)}$ are independent vectors of law $\mathcal{N}(0, I_{2l})$, the real-valued vectors $Z^{(1)}$ and $Z^{(2)}$ defined by

$$Z^{(1)} + iZ^{(2)} = \frac{1}{\sqrt{2l}} \cdot F_{2l}^* \operatorname{diag}(F_{2l} s_H(l))^{1/2} \, (\varepsilon_{2l}^{(1)} + i\varepsilon_{2l}^{(1)})$$

are independent with common law $\mathcal{N}(0, S_H(l))$. In particular, one has $(Z_H(0), \ldots, Z_H(l)) \stackrel{d}{=} (Z_0^{(i)}, \ldots, Z_l^{(i)})$ for $i = 1, 2$, and using stationarity of the increments of B_H and the fact that $B_H(0) = 0$ a.s., one has, for all $m \leq l$,

$$(B_H(k))_{-m \leq k \leq l-m} = \left(\sum_{j<k+m} Z_H(j) - \sum_{j<m} Z_H(j) \right)_{-m \leq k \leq l-m},$$

with the convention that $\sum_{j<0} = 0$. Let us emphasize that this procedure is very fast since, choosing l as a power of 2, the cost is reduced to $C(l) = O(2^{\lceil \log_2(l) \rceil} \lceil \log_2(l) \rceil)$, where $\lceil x \rceil$ denotes the upper integer part of x, using the Fast Fourier Transform algorithm. It follows that the cost is similar to that of the spectral method but with the considerable advantage that the resulting simulations are exact and not approximate.

Appendix B: Optimal band selection algorithm based on Dynamic Programming

input : α_1, α_2, defining the considered angular interval
ε: the maximum angular distance between two adjacent bands
r: resolution parameter (the sampling step is $1/r$)
output: a finite sequence of integer vectors $(\bar{p}_k, \bar{q}_k)_{1\leq k\leq s}$

$N \leftarrow 1 + \lceil \frac{1}{\tan \varepsilon} \rceil$
Build the set $\mathcal{V}$ of all integer vectors $(q,p) \in \{1,\dots,N\} \times \{-N,\dots,N\}$ such that $\gcd(p,q) = 1$ and $\alpha_1 < \arctan \frac{p}{q} < \alpha_2$
Sort $\mathcal{V}$ into a sequence $(p_k, q_k)_{1\leq k\leq n}$ with $k \mapsto \theta_k := \arctan \frac{p_k}{q_k}$ increasing
Compute the cost e_k associated to each (q_k, p_k)
Add extremal angles: $\theta_0 \leftarrow \alpha_1$ ($e_0 \leftarrow 0$) and $\theta_{n+1} \leftarrow \alpha_2$
$c_{n+1} \leftarrow 0$
for $i = n, n-1, \dots 0$ **do**
    $cmin \leftarrow \infty$
    $j \leftarrow i+1$
    while $j \leq n+1$ *and* $\theta_j \leq \theta_i + \varepsilon$ **do**
        if $c_j \leq cmin$ **then**
            $cmin \leftarrow c_j$
            $k_i \leftarrow j$
        end
        $j \leftarrow j+1$
    end
    $c_i \leftarrow e_i + cmin$
end
$i \leftarrow 0$
$s \leftarrow 0$
while $i \leq n$ **do**
    $i \leftarrow k_i$
    $s \leftarrow s+1$
    $(\bar{p}_s, \bar{q}_s) \leftarrow (p_i, q_i)$
end
`return` $(\bar{p}_k, \bar{q}_k)_{1\leq k\leq s}$

References

Dietrich, C. and Newsam, G. (1997). Fast and exact simulation of stationary Gaussian processes through circulant embedding of the covariance matrix. *SIAM J Sci Comput*, **18**(4), 1088–1107.

Perrin, E., Harba, R., Jennane, R., and Iribarren, I. (2002). Fast and exact synthesis for 1-D fractional Brownian motion and fractional Gaussian noises. *IEEE Signal Process Lett*, **9**(11), 382–384.

[1] LMA, CNRS UMR 7348, Université Poitiers, Téléport 2-BP30179, Boulevard Marie et Pierre Curie, 86962 Chasseneuil Cedex, France. *E-mail address*: hermine.bierme@math.univ-poitiers.fr

[2] Université Paris Descartes, MAP5, CNRS UMR 8145, Sorbonne Paris Cité, 45 rue des Saints-Pères, 75006 Paris, France. *E-mail address*: lionel.moisan@parisdescartes.fr

[3] Aix Marseille Université, CNRS, Centrale Marseille, I2M, UMR 7373, 13453 Marseille, France. *E-mail address*: frederic.richard@univ-amu.fr